

# Hibernating black holes revealed by photometric mass functions

Jorge Casares<sup>1,2,3</sup>★†

<sup>1</sup>*Instituto de Astrofísica de Canarias, 38205 La Laguna, Tenerife, Spain*

<sup>2</sup>*Departamento de Astrofísica, Universidad de La Laguna, E-38206 La Laguna, Tenerife, Spain*

<sup>3</sup>*Department of Physics, Astrophysics, University of Oxford, Keble Road, Oxford OX1 3RH, UK*

Accepted XXX. Received YYY; in original form ZZZ

## ABSTRACT

We present a novel strategy to uncover the Galactic population of quiescent black holes (BHs). This is based on a new concept, the *photometric mass function* (PMF), which opens up the possibility of an efficient identification of dynamical BHs in large fields-of-view. This exploits the width of the disc H $\alpha$  emission line, combined with orbital period information. We here show that H $\alpha$  widths can be recovered using a combination of customized H $\alpha$  filters. By setting a width cut-off at 2200 km s<sup>-1</sup> we are able to cleanly remove other Galactic populations of H $\alpha$  emitters, including  $\sim$ 99.9% of cataclysmic variables (CVs). Only short period ( $P_{\text{orb}} < 2.1$  h) eclipsing CVs and AGNs will contaminate the sample but these can be easily flagged through photometric variability and, in the latter case, also mid-IR colours. We also describe the strategy of a deep ( $r=22$ ) Galactic plane survey based on the concept of PMFs: *HAWKs*, the *HAlpha-Width Kilo-deg* Survey. We estimate that  $\sim$ 800 deg<sup>2</sup> are required to unveil  $\sim$ 50 new dynamical BHs, a three-fold improvement over the known population. For comparison, a century would be needed to produce an enlarged sample of 50 dynamical BHs from X-ray transients at the current discovery rate.

**Key words:** accretion, accretion discs – X-rays: binaries – stars: black holes – novae: cataclysmic variables

## 1 INTRODUCTION

The historic discovery of gravitational waves (GW) from merging BHs has undoubtedly opened a new era in astronomy (Abbott et al. 2016a,b). It means that BHs can now be detected without an electromagnetic counterpart. Also, the prediction of  $\sim 10^3$  new merging BHs to be discovered by Advanced LIGO in the next decade will allow for the first BH demographic studies across cosmological times (Abbott et al. 2016c; Sesana 2016; Kovetz et al. 2017; Cholis 2017; Elbert et al. 2017). Different formation scenarios, however, have been proposed to explain the GW events GW150914 and GW151226, including massive binaries at low metallicity, dynamical encounters in globular clusters or primordial BHs (Belczynski et al. 2016; De Mink & Mandel 2016; Rodriguez et al. 2016; Coleman Miller 2016; Clesse & García-Bellido 2017). At present it is unclear which model can better accommodate the new GW BHs and it seems likely that a degenerate combination of multiple formation channels may

be responsible for the entire population. In this context, the study of BHs in Galactic X-ray binaries remains extremely valuable because they present us with a homogeneous reference sample, drawn from a very specific formation channel in solar metallicity environment (e.g. Wang et al. 2016 and references therein). This is precisely the scope of the current paper.

Galactic BHs are mostly discovered in X-ray transients (XRTs), a subclass of X-ray binaries which exhibit episodic outbursts triggered by accretion disc instabilities (see e.g. Belloni et al. 2011). These X-ray brightenings can be dramatic as they happen within a day or so, and can often outshine the brightest sources in the sky, making them easy to spot by X-ray monitoring satellites. But between these extraordinary outbursts, BH XRTs *hibernate* in a “quiescent” state, which can last for several decades or more, with typical X-ray luminosities below  $\sim 10^{32}$  erg s<sup>-1</sup>. It is during these times that it becomes possible to detect the faint low-mass donor star at optical/NIR wavelengths and exploit its kinematics to constrain the masses of the binary components. About 60 XRTs with suspected BHs (as indicated by their X-ray timing and spectral properties) have been

★ Leverhulme Visiting Professor

† E-mail: jorge.casares@iac.es

discovered since the dawn of X-ray astronomy but most of them faded below the detection threshold of present instrumentation during their decay (Corral-Santana et al. 2016). Time-resolved spectroscopy in quiescence is required for dynamical confirmation (i.e. a mass function greater than  $\sim 3 M_{\odot}$ ) and this has only been achieved in  $\sim 50$  years for 17 BH transients (Casares & Jonker 2014). For detailed population studies it is therefore critical to dramatically increase the number of dynamical BHs in X-ray binaries. This requires a new research methodology rather than simply waiting for new transients to trigger an outburst, as this would take many decades to barely double the current number.

In this regard, lessons can be learned from the study of supermassive BHs in quasars (QSOs) and Active Galactic Nuclei (AGNs). Nearby supermassive BHs are also weighed from the kinematics of central stars or, in exceptional circumstances, water radio masers. However, in distant galaxies, when the BH radius of influence cannot be resolved, empirical scalings with galaxy properties (such as the  $M_{\text{BH}}-\sigma$  relation in the bulge and others based on reverberation mapping of the broad-line region, BLR) have to be applied (see Kormendy & Ho 2013 for a review of the different methods). In the most frequent form of reverberation-based techniques, the BH mass scales with the width of emission-lines formed in the BLR and the continuum luminosity, a proxy for the BLR size (Peterson et al. 2004; Vestergaard & Peterson 2006). Similarly, when the donor star is not detected in quiescent XRTs, scaling relations of spectral features with fundamental binary parameters may prove useful. For example, in Casares (2016) (Paper II hereafter), we show that the ratio between the double-peak separation and the FWHM of the  $H\alpha$  line, formed in the accretion disc, correlates with the binary mass ratio  $q = M_2/M_1$  for  $q \lesssim 0.25$  (with  $M_2$  and  $M_1$  being the masses of the companion and BH, respectively). This stems from the fact that the double peak separation traces the outer disc truncation radius which, for these extreme mass ratios, is determined by the 3:1 resonance tide with the companion star. The relation presented in Paper II can, for instance, provide a first estimate of the BH mass when  $M_2$  is inferred from broad-band colors or the orbital period (assuming the companion is a Roche-lobe filling Main Sequence star dominating the quiescent optical/NIR spectrum).

Furthermore, in Casares (2015) (hereafter Paper I) we find that the FWHM of the  $H\alpha$  line scales with the projected velocity semi-amplitude of the companion star  $K_2$ , i.e. <sup>1</sup>

$$K_2 = 0.233 \text{ FWHM} \quad (1)$$

This equation suggests a fundamental scaling between the dynamics of the gas in the accretion disc and the companion star. It should be mentioned that the slope of the FWHM-K2 correlation does contain a weak dependence on  $q$  (see eqs. 5-6 in Paper I); for example, cataclysmic variables above

<sup>1</sup> Note that a precursor of this equation was presented in Warner (1973) (see also Jurcevic et al. 1994). These earlier versions were developed for the case of cataclysmic variables (i.e. interacting binaries with accreting white dwarfs) although, at variance with equation (1), provide a scaling with the projected velocity of the primary star,  $K_1$ , as inferred from the motion of the wings of the  $H\beta$  line.

the period gap display a  $\sim 27\%$  flatter slope than shown by equation (1). In any case, the FWHM-K2 correlation deploys very tightly for BH XRTs because their mass ratios cluster within a very narrow range centered at  $q \sim 0.05$ .

As a matter of fact, equation (1) proves very useful to study faint XRTs: it simply requires resolving the width of the  $H\alpha$  line (usually the strongest feature in the spectrum) rather than measuring the doppler shifts of weak absorption lines from the donor star in phased-resolved spectra. Therefore, if the orbital period is known (e.g. through photometric variability) then mass functions can be extracted from single-epoch spectroscopy. This effectively allows extending dynamical studies to XRTs  $\sim 2$  magnitudes fainter than is currently possible, anticipating what 40-m class telescopes can achieve in the next decade using traditional techniques. Examples of this strategy are presented in Zurita et al. (2015), Mata-Sánchez et al. (2015) and Torres et al. (in preparation), see also Paper II.

In addition, Paper I introduces a new concept, the *photometric mass function* (PMF), expressed by

$$\left(\frac{\text{PMF}}{M_{\odot}}\right) \equiv 1.3 \times 10^{-9} \left(\frac{P_{\text{orb}}}{d}\right) \left(\frac{\text{FWHM}}{\text{km s}^{-1}}\right)^3 = \left(\frac{M_1}{M_{\odot}}\right) \frac{\sin^3 i}{(1+q)^2} \quad (2)$$

Here PMF refers to the case when both  $H\alpha$  widths (i.e. FWHM) and orbital periods ( $P_{\text{orb}}$ ) are derived *photometrically*. Since mass functions provide a lower limit to the mass of the accreting star, PMFs (as delivered by imaging techniques) can be exploited to discover quiescent BHs very efficiently in large fields of view.

In this paper we present a proof-of-concept on how  $H\alpha$  FWHMs can be measured through photometry using custom interference filters, and how this can be exploited to filter out contaminating sources that plague classic  $H\alpha$  surveys (Section 2). In Section 3 we propose a survey strategy to identify hibernating BHs from  $H\alpha$  widths and PMF selection. Finally, in Sections 4 and 5 we discuss our results and summarize the conclusions. We envision that this new methodology has the potential for boosting the statistics of dynamical BHs by an order of magnitude within only a few years.

## 2 A PHOTOMETRIC SYSTEM TO MEASURE $H\alpha$ WIDTHS

Dormant BH XRTs are very difficult to identify because of their extremely low accretion luminosities. In turn, the companion (typically a K-type star) dominates the optical spectrum, thereby effectively disguising quiescent XRTs amongst the myriad of field stars. Only the presence of superimposed broad emission lines from the accretion disc, most notably  $H\alpha$ , can betray their presence. In fact, current  $H\alpha$  surveys of the Galactic plane, such as the *SuperCOSMOS H-alpha Survey* (SSH, Parker et al. 2005) or the *INT Photometric H-alpha Survey of the Northern Galactic Plane* (IPHAS, Drew et al. 2005) might contain quiescent BHs but, unfortunately, they are vastly outnumbered by other populations of  $H\alpha$  emitters such as symbiotic binaries, cataclysmic variables (CVs), Be stars or planetary nebulae. For example, among the  $\sim 10^4$   $H\alpha$  sources contained in

IPHAS (Drew et al. 2005; Witham et al. 2008) no BH candidates have yet been produced. Another approach, followed by the *Galactic Bulge Survey* (GBS) relies mainly on cross-matching H $\alpha$  emitting objects with weak X-ray sources from a shallow Chandra survey of the Galactic Bulge (Jonker et al. 2011, 2014). About 25 new quiescent BHs were predicted by GBs but only intervening CVs (mostly magnetic), W UMa or coronally active stars have been securely identified so far (e.g. Torres et al. 2014; Wevers et al. 2017).

Here we propose a new route that exploits the width of the H $\alpha$  line as a tracer of the strong gravitational field exclusive to BHs. From the compilation presented in Paper I we note that quiescent BHs typically possess FWHM  $\gtrsim 1000$  km s $^{-1}$ , i.e. much larger than observed in most other populations of H $\alpha$  emitters. Therefore, in order to flush out potential contaminants it would be of great interest to develop a photometric system tailored to measure H $\alpha$  line widths. In principle, this could be achieved with just a pair of H $\alpha$  interference filters: one sufficiently broad to contain the entire line flux (hereafter called H $\alpha$  *broad*, H $\alpha_b$ ) and another filter matched to sample only the line core (H $\alpha$  *narrow*, H $\alpha_n$ ). To test this idea we have simulated a pair of H $\alpha_b$  and H $\alpha_n$  filters by scaling filter #197 from the Wide Field Camera (WFC) on the 2.5m Isaac Newton Telescope (INT), which has an effective FWHM of 95 Å<sup>2</sup>. The two simulated filters have been shifted to the H $\alpha$  rest wavelength i.e. 6562.76 Å. For the H $\alpha_b$  filter we take a bandwidth of 150 Å so as to encompass the entire flux of the broadest BH H $\alpha$  line currently known i.e. that of Swift J1357-0933 (Paper I). Regarding the H $\alpha_n$  filter we start by adopting a bandwidth of 33 Å (=1508 km s $^{-1}$ ). In addition, we have produced a set of synthetic "interacting binary" spectra consisting of double-peaked H $\alpha$  profiles with fixed EW=50 Å (we take EWs of emission lines as positive henceforth) and FWHM=670-4450 km s $^{-1}$  sitting on a red-denied linear continuum (Appendix A). In the top panel of Figure 1 we present the synthetic spectra, together with the transmission curves of the simulated filters.

The synthetic spectra were convolved with the transmission curves of the H $\alpha_b$  and H $\alpha_n$  filters and integrated over wavelength to derive associated fluxes (Appendix A). Here and henceforth, we sample the filter's response curves and the spectra to a common wavelength scale of 1 Å pix $^{-1}$ . The bottom panel in Figure 1 displays the ratio of fluxes obtained from the pair of H $\alpha$  filters as a function of line FWHM. The latter was derived through fitting Gaussian functions to the synthetic profiles (see Appendix A). The smooth curve indicates that FWHM values can indeed be recovered from the combined fluxes provided by the simulated filters. We subsequently applied the same exercise to a sample of flux-calibrated spectra of BHs and CVs from the compilation presented in Paper I<sup>3</sup> and the result is presented in Figure 2. This time the smooth trend is replaced by significant scatter, caused by large variations in line EW from system

<sup>2</sup> The transmission curve of this filter is available from <http://catserver.ing.iac.es/filter/filtercurve.php?format=tst&filter=197>

<sup>3</sup> The sample contains 9 BHs (V404 Cyg, BW Cir, GRO J0422+320, XTE J1650-50, N. Oph 77, A0620-00, GS2000+25, XTE J1118+480, Swift J1357-0933) and 4 CVs (CH UMa, SS Aur, SS Cyg, U Gem) covering a wide range of FWHMs between 600 and 4200 km s $^{-1}$ . Spectral fluxes have been normalized to the continuum level at H $\alpha$ .

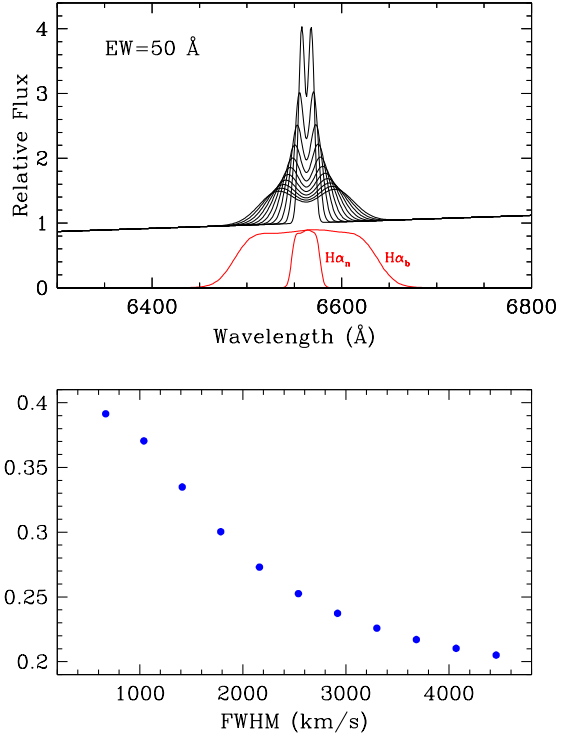


**Figure 1.** Top: Synthetic double-peaked H $\alpha$  spectra with FWHM=670-4450 km s $^{-1}$ , together with the transmission curves of our simulated H $\alpha$  filters. Bottom: Variation of the filter's flux ratio versus FWHM. The flux ratio is computed through the convolution of the synthetic spectra with the H $\alpha$  filters.

to system. This can be interpreted as the effect of different underlying continua diluting the contribution of the line to the total flux. In other words, a broad emission line sitting on a strong continuum can mimic the same flux ratio as a narrow line over a weak continuum. Therefore, in order to measure accurate line widths it is crucial to know the EW of the line beforehand and this can be accomplished with an extra observation using a broader filter (r-band hereafter), also centered at H $\alpha$ .

## 2.1 Photometric EWs

It is easy to prove that the EW of an H $\alpha$  line can be approximated by the following equation

$$EW_{ph} = C_1 \frac{W_r \times \left( \frac{F_{H\alpha_b}}{F_r} \right) - W_{H\alpha_b}}{1 - \left( \frac{F_{H\alpha_b}}{F_r} \right)} \quad (3)$$

where  $W_{H\alpha_b}$  and  $W_r$  stand for the equivalent widths of the H $\alpha_b$  and r-band filters,  $F_{H\alpha_b}$  and  $F_r$  are the fluxes measured by the filters and  $C_1$  a calibration constant (see Appendix B). We call this expression  $EW_{ph}$  or *photometric EW* i.e. the EW as derived from observations with the two photometric filters. Here again we have simulated the r-band filter by scaling filter #197 of the WFC to a bandwidth

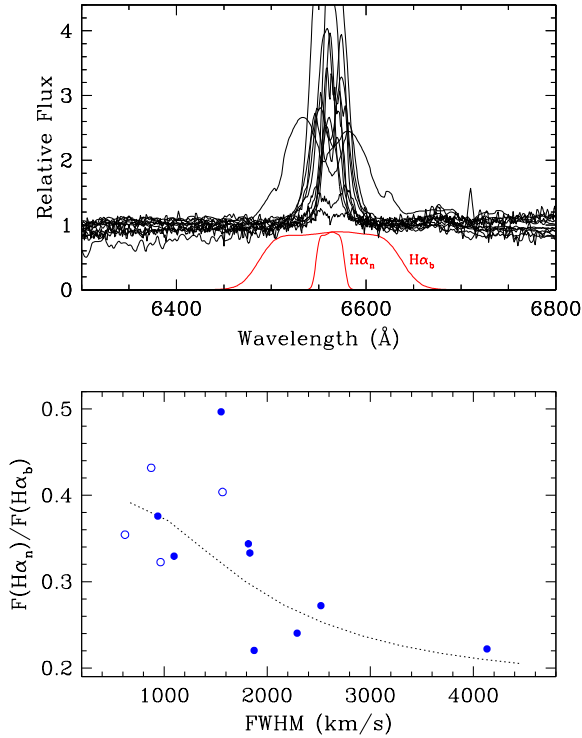


**Figure 2.** Same as Figure 1 but for a sample of 9 BH (filled circles) and 4 CV (open circles) real spectra. Error bars in the lower panel are smaller than the symbol size and are not displayed. The dotted line indicates the trend derived from synthetic spectra, with  $EW=50$  Å.

of 550 Å and an effective central wavelength of 6562.76 Å. The width of the r-band filter was adopted to avoid the strong telluric O I emission line at  $\lambda 6300$  and the B-band absorption at  $\sim 6860$  Å, which may affect the accuracy of photometric measurements. In the specific case of our filters we find  $W_{H\alpha_b} = 132.7$  Å and  $W_r = 487.0$  Å through integration of the filter’s transmission curves. In order to determine  $C_1$  we created a set of synthetic X-ray binary spectra with  $FWHM=2500$  km s<sup>-1</sup> and EWs in the range 10–250 Å. These were subsequently convolved with the transmission curves of the filters to yield  $F_{H\alpha_b}$  and  $F_r$  fluxes.  $EW_{ph}$  values are then computed through equation 3 and compared to model EWs. A linear fit to the sequence of  $EW_{ph}$  and model EW values leads to  $C_1 = 1.155$ . The results are displayed in Figure 3.

## 2.2 Photometric FWHMs

Once  $EW_{ph}$  is determined, it is then possible to extract the FWHM of the line through the expression

$$FWHM_{ph} = C_2 \frac{EW_{ph}}{\left(\frac{EW_{ph} + W_{H\alpha_b}}{W_{H\alpha_n}}\right) \times \left(\frac{F_{H\alpha_n}}{F_{H\alpha_b}}\right) - 1} \quad (4)$$

where  $W_{H\alpha_n}$  is the equivalent width of the Hα<sub>n</sub> filter ( $W_{H\alpha_n} = 26.3$  Å in our case),  $F_{H\alpha_n}$  the flux measured

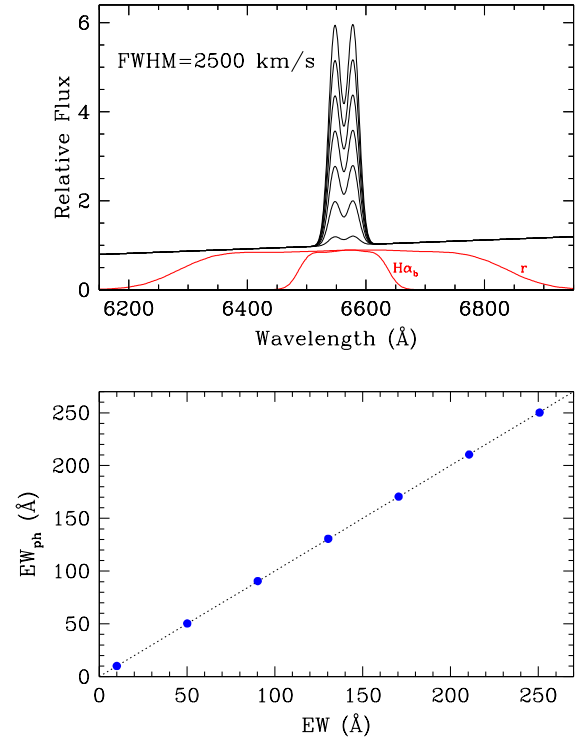


**Figure 3.** Top: Synthetic double-peaked Hα spectra with  $FWHM=2500$  km s<sup>-1</sup> and different EWs in the range 10–250 Å, together with the transmission curves of our simulated Hα<sub>b</sub> and r-band filters. Bottom: Photometric EWs ( $EW_{ph}$ ), as extracted from equation 3 with  $C_1 = 1.155$ , versus model EWs. The dotted line represents  $EW_{ph} = EW$ .

through that filter and  $C_2$  a calibration constant (see Appendix C). In the same way as before,  $C_2$  has been obtained by comparing FWHM values of synthetic spectra (with fixed  $EW=50$  Å, see top panel in Figure 4) with  $FWHM_{ph}$  values computed from equation 4, resulting in  $C_2 = 0.826$ . The bottom panel of Figure 4 displays the behaviour of  $FWHM_{ph}$  versus model FWHMs for a grid of synthetic spectra with  $EW=10$ –150 Å and  $FWHM=670$ –4450 km s<sup>-1</sup>. The figure demonstrates that FWHMs are now uniquely determined through equation 4, irrespectively of the line EW. Only at small widths  $\leq 1200$  km s<sup>-1</sup> do the  $FWHM_{ph}$  values deviate significantly from model FWHMs but this is only because we are limited by the bandwidth of the narrow Hα filter which determines our effective resolution in width.

A final test is performed with our previous sample of real BH and CV spectra and the results are presented in Figure 5. In contrast to Figure 2, the variations in line EW are now accounted for, allowing us to recover line widths at <5% accuracy for  $FWHM \geq 1200$  km s<sup>-1</sup>. Here 5% indicates the largest fractional difference between the true data FWHM and the  $FWHM_{ph}$  values provided by eq. 4. Therefore, photometric observations with a combination of only three filters (broadband r plus two narrowband Hα filters) are sufficient to determine the width (and equivalent width) of the Hα line in quiescent BH XRTs.

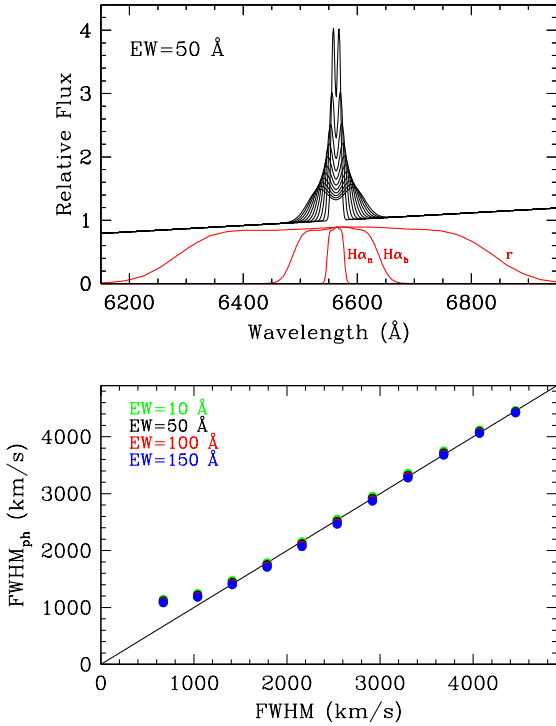


**Figure 4.** Top: Example synthetic double-peaked H $\alpha$  spectra with EW=50 Å and FWHM in the range 670-4450 km s<sup>-1</sup>, together with the transmission curves of our simulated H $\alpha_n$ , H $\alpha_b$  and r-band filters. Bottom: Photometric FWHMs (FWHM<sub>ph</sub>), as provided by equation 4 with  $C_2 = 0.826$ , versus FWHMs measured through a Gaussian fit for different model EWs in the range 10-150 Å. The dotted line represents FWHM<sub>ph</sub> = FWHM. Note that only spectra with FWHM  $\leq$  1200 km s<sup>-1</sup> deviate from the line because their widths are smaller than the bandwidth of the narrow H $\alpha$  filter.

### 2.3 Width Cut-off for BH selection

Having proved that line FWHMs can be reliably measured with our photometric system we now need to define an optimal width cut-off to efficiently select quiescent BHs. This is an important issue as it determines the fraction of other H $\alpha$  emitting objects that will be rejected. Larger cut-off widths will filter out narrow H $\alpha$  emitters but also BHs at lower inclinations and, therefore, a compromise must be devised. For example, a cut-off at FWHM  $\sim$  1500 km s<sup>-1</sup> will instantly clean out most potential contaminants such as T Tau, Be stars, chromospherically active stars or planetary nebulae. Only CVs at moderately high inclinations can produce H $\alpha$  lines this broad because of the deep potential wells of their accreting white dwarfs. However, with a Galactic density of  $\sim 10^4$  kpc<sup>-3</sup> (Pretorius & Knigge 2012, see also Burenin et al. 2016 for an update based on recent constraints on the X-ray luminosity function) CVs are a factor  $\approx 10^3$  more numerous than BH XRTs (e.g. Corral-Santana et al. 2016) and most likely will dominate the Galactic population of H $\alpha$  contaminants, even at these large widths. So it is

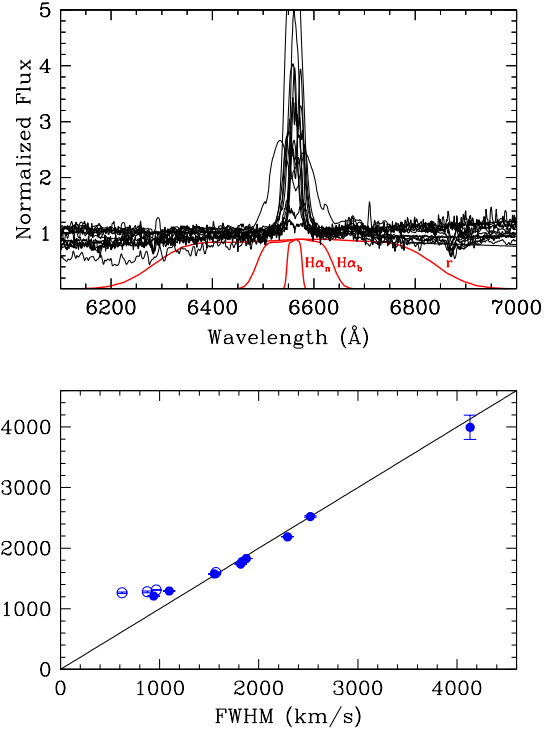


**Figure 5.** Same as Figure 4 but for a sample of 9 BHs (filled circles) and 4 CVs (open circles). Error bars in the lower panel are smaller than the symbol size in all but one case. Photometric widths recover real FWHMs to better than 5% for FWHM  $\geq$  1200 km s<sup>-1</sup>.

important to set a more stringent width cut-off in order to optimize the rejection of potentially contaminating CVs.

To investigate this issue we have run Monte Carlo simulations ( $10^5$  trials) of the expected distribution of FWHMs for the two binary populations. In the case of BH XRTs we have computed FWHMs from equation 2, assuming an isotropic distribution of inclinations i.e.  $\langle \cos i \rangle = 0.5$ . Following Özel et al. (2010) we have drawn BH masses from a normal distribution with mean 7.8  $M_\odot$  and  $\sigma = 1.2 M_\odot$ .  $P_{\text{orb}}$  and  $q$  values are also obtained from normal distributions with  $\langle P_{\text{orb}} \rangle = 0.287$  d,  $\sigma(P_{\text{orb}}) = 0.14$ ,  $\langle q \rangle = 0.05$  and  $\sigma(q) = 0.02$ . These have been parametrized from Gaussian fits to the observed distributions of  $P_{\text{orb}}$  and mass ratios in BH XRTs (Figure 6), as listed in Casares & Jonker (2014) and Paper II. The sample also includes the orbital periods of Swift J1753.5-0127 (Zurita et al. 2008), Swift J1357.2-0933 (Corral-Santana et al. 2013) and MAXI J1650-152 (Kuulkers et al. 2013), the shortest currently known. Note that BH XRTs with intermediate-mass donor stars (i.e. XTE J1819.3-2525, GRO J1655-40 and 4U 1543-475, all with  $P_{\text{orb}} \approx 1 - 3$  d and  $q \gtrsim 0.3$ ) are not considered because of the lack of H $\alpha$  emission in their spectra. Finally, the area of the FWHM probability distribution function (PDF) has been scaled by a factor 1000 to account for the larger size of the Galactic population of CVs relative to BH XRTs.

For the case of CVs, we start by assuming the  $P_{\text{orb}}$  dis-



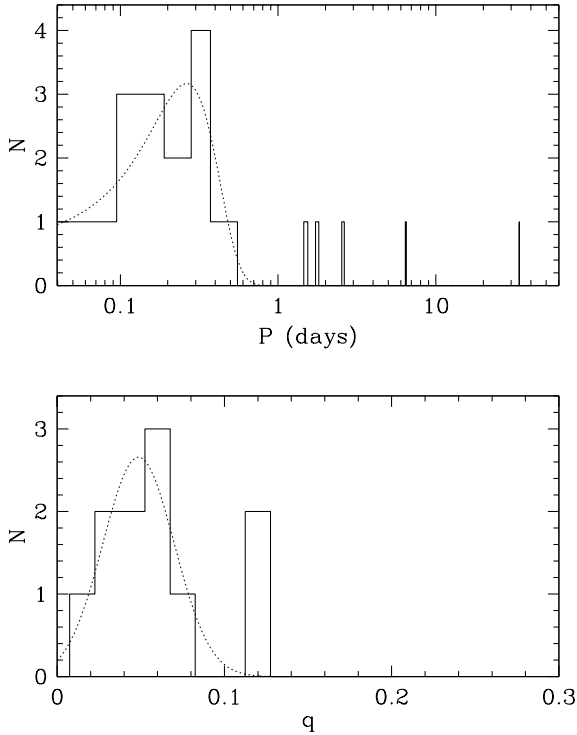


**Figure 6.** Observed distribution of orbital periods (top) and mass ratios (bottom) for BH XRTs. The dotted line represents the best Gaussian fit.

tribution of the 1146 CVs listed in the 7th edition of the [Ritter & Kolb \(2003\)](#) catalogue (Release 7.21). This contains the sample of intrinsically faint short-period CVs discovered by Sloan ([Gänsicke et al. 2009](#)) and will be referred to as *model CV-1* henceforth. The ultracompact AM CVn binaries are excluded because they possess degenerate donor stars and, therefore, they lack Balmer emission lines. Since mass ratios are known to increase with  $P_{\text{orb}}$  (e.g. [Knigge et al. 2011](#)), we adopted an exponential dependence of the form  $q = 0.731 - 11.55 \times e^{-(P_{\text{orb}}+0.388)/0.154}$ , derived through a least-square fit to 117 pairs of  $P_{\text{orb}}-q$  values from [Ritter & Kolb \(2003\)](#). White dwarf masses are drawn from a normal distribution with mean= $0.83 M_{\odot}$  and  $\sigma = 0.23 M_{\odot}$  ([Zorotovic et al. 2011](#)), while binary inclinations are also assumed to be randomly distributed. As before,  $P_{\text{orb}}$ ,  $q$ ,  $M_1$  and  $\cos i$  values are used as inputs to equation 2, with one proviso: because of the wide range of  $q$  values for CVs we do not assume the FWHM- $K_2$  scaling from equation 1 but the more general expressions given by equations 5 and 6 in Paper I, with  $\alpha = 0.42$ .

The number of CVs below the period gap in model CV-1 is a factor  $\sim 2$  larger than those above the gap. This fraction, however, is most likely biased low by selection effects ([Gänsicke 2005](#)) and hence we decided to compute a further PDF distribution where, following the prediction of standard CV population models, we have incremented the number of CVs below the gap to 98% of the total population ([Kolb 1993](#); [Howell et al. 2001](#); [Knigge et al. 2011](#)). We call this

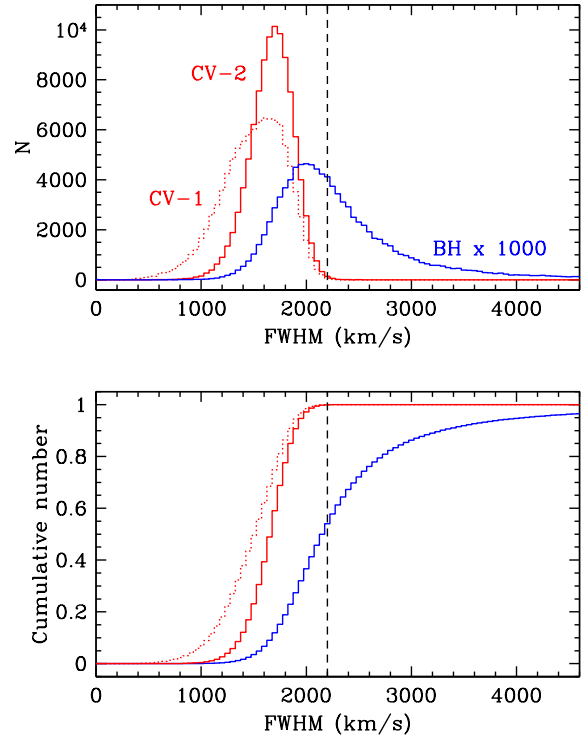


**Figure 7.** Top: Monte Carlo PDFs of FWHMs for BHs and CVs (models 1 and 2). For the sake of display, the BH distribution has been enlarged by a factor 1000. The dashed vertical line at  $\text{FWHM}=2200 \text{ km s}^{-1}$  marks our selected cut-off width. Bottom: Normalized cumulative distributions of the number of CVs and BHs as a function of FWHM. A width cut-off at  $\text{FWHM}=2200 \text{ km s}^{-1}$  allows selecting  $\sim 46\%$  of BHs while rejecting  $\sim 99.9\%$  of CVs.

*model CV-2* and take it as a more realistic representation of the true Galactic population of CVs. Figure 7 presents the PDFs of the FWHM and their cumulative distribution functions for BHs and the two CV models, while Table 3 lists the percentage of the total populations selected by specific FWHM cut-off values. Because of the larger number of short period CVs in model CV-2, the fraction rejected by a given cut-off will be lower than in model CV-1. Since CVs are  $\approx 10^3$  times more abundant than BHs, we tentatively adopt  $\text{FWHM}>2200 \text{ km s}^{-1}$  as our optimal cut-off value. According to the simulation, this cut-off would allow the rejection of  $\sim 99.9\%$  of CVs while retaining  $\sim 46\%$  of BHs i.e. under the assumption of equal absolute magnitudes and Galactic distributions it would select  $\approx 2$  CVs per BH discovered.

## 2.4 The $H\alpha$ Colour Diagram

For practical purposes, Figure 8 presents a colour-colour diagram constructed using the simulated filters described in Sections 2.1 and 2.2. We call this the *H $\alpha$  Colour Diagram* and contains the information on FWHM and EW of  $H\alpha$  emitting stars. To guide the eye, lines of constant FWHM and EW are overplotted, as calculated through con-

evolution of synthetic double-peaked profiles with our filter transmission curves (see Appendix A). A line of maximum FWHM has been drawn at  $5400 \text{ km s}^{-1}$ , based on the extreme case of a  $12 M_{\odot}$  BH with a  $0.07 M_{\odot}$  companion star (right at the H-burning limit) in a 1.37 hr orbit, seen edge-on ( $i = 90^{\circ}$ ). This orbital period has been derived assuming that the companion star fills its Roche lobe and obeys the semi-empirical Mass-Radius relations from Knigge et al. (2011). Our width cut-off at  $\text{FWHM}=2200 \text{ km s}^{-1}$  is indicated by the blue continuous line. The optimum region for BH detection in the  $\text{H}\alpha$  Colour Diagram is hence restricted between the  $\text{FWHM}=2200$  and  $5400 \text{ km s}^{-1}$  lines. For comparison, we have plotted in blue circles synthetic colours of our sample of dynamical BHs while 285 bona-fide CVs, selected from Sloan DR7 (Szkody et al. 2011), have been marked by red triangles. Because of the survey depth and broad colour selection cuts Sloan CVs provide the least biased sample obtained so far (see Gänsicke 2005) and hence we take these as the best representation of the field CV population that one might expect to find. Finally, synthetic colours of a grid of O-M Main Sequence, Giants and Supergiant stars from Jacoby et al. (1984) are also plotted as green crosses.

We note that  $\text{H}\alpha$  emitters are cleanly segregated in this diagram from non- $\text{H}\alpha$  emitting field stars. The latter tend to cluster at  $\text{EW}\approx 0$ , i.e. near the focus of lines of constant FWHM, with some spreading along two characteristic directions: (1) a tail towards  $\text{EW} < 0$  and large FWHMs, produced by A-B stars with broad  $\text{H}\alpha$  absorptions (also a locus for isolated DA white dwarfs and CVs in outburst) and (2) a vertical stream at  $\text{FWHM}\sim 5400 \text{ km s}^{-1}$  and  $\text{EW}\sim 0 - 50 \text{ \AA}$ , caused by M-type stars (mostly Giants and Supergiants) with deep molecular bands. It should be noted that, because our three filters are relatively narrow and have a common central wavelength, this diagram is insensitive to reddening. Therefore, stellar positions do not depend on extinction and both EWs and FWHMs of  $\text{H}\alpha$  lines are uniquely determined, irrespectively of the slope of the underlying continuum. This represents a clear advantage over other  $\text{H}\alpha$  surveys based on broad band colours, where EWs often become degenerate with interstellar extinction and the spectral energy distribution of the star (see e.g. Drew et al. 2005).

The  $\text{H}\alpha$  colour diagram proves that the great majority of Sloan CVs are nicely rejected by the  $\text{FWHM}=2200 \text{ km s}^{-1}$  cut-off, with only three exceptions: DV UMa, IY UMa and SDSS J122740.83+513925.0. These three CVs are eclipsing and have orbital periods in the range 1.52-2.06 hr. As a matter of fact, only CVs with very short orbital periods and extreme inclinations (thus eclipsing) are able to produce  $\text{H}\alpha$  lines broader than  $\text{FWHM}\geq 2200 \text{ km s}^{-1}$ . This is exemplified by Figure 9, where we display FWHMs of  $\text{H}\alpha$  lines versus  $P_{\text{orb}}$  for the sample of dynamical BHs (blue circles) and CVs (red solid triangles) presented in Paper I. Eclipsing CVs are distinguished by red open triangles. A recent determination of the FWHM of  $\text{H}\alpha$  for MAXI J1659-152 has also been included (Torres et al. in preparation). The continuous black line represents a hard upper limit on FWHM for CVs, as obtained from the PMF expression (eq. 2), assuming maximum inclination  $i = 90^{\circ}$  and the Chandrasekhar mass limit, combined with the  $P_{\text{orb}} - q$  dependence derived in Section 2.3 and equations 5 and 6 from Paper I. In addition, we draw in dashed line style a lower limit for eclipses of the accretion disc. This has been obtained in the same

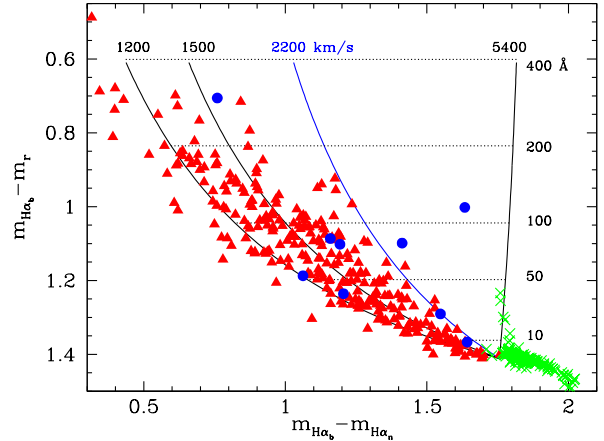


**Figure 8.** The  $\text{H}\alpha$  colour-colour diagram. Dotted horizontal lines represent constant EWs in the range 10-400  $\text{\AA}$  while vertically curved continuous lines indicate constant FWHM in the range 1200-5400  $\text{km s}^{-1}$ . The blue line at  $\text{FWHM}=2200 \text{ km s}^{-1}$  marks our favored width cut-off for efficient BH selection. SDSS CVs are located by red triangles, BH XRTs by blue dots and spectral type standards of luminosity class I, III and V by green stars.

way as before albeit for a typical white dwarf mass of  $0.83 M_{\odot}$  (Zorotovic et al. 2011) and the eclipse condition

$$\cos i \geq \left[ \left( \frac{R_d}{R_{L1}} \right) + \frac{1 - \left( \frac{R_d}{R_{L1}} \right)}{0.462} \times \left( \frac{1+q}{q} \right)^{1/3} \right]^{-1} \quad (5)$$

with  $R_d/R_{L1} = 0.5$  i.e. the accretion disc radius extending to 0.5 times the primary Roche lobe (e.g. Marsh et al. 1994). This expression is derived from simple geometry using Paczyński's approximation for the radius of the companion's Roche lobe (Paczynski 1971). The vertical dotted lines mark the extremes of the period gap, between 2.15 hr and 3.18 hr. Figure 9 demonstrates that only eclipsing CVs with  $P_{\text{orb}}$  under the gap are able to produce  $\text{H}\alpha$  lines broader than  $2200 \text{ km s}^{-1}$ . Therefore, those CVs not rejected by our width cut-off will be easily identified from the presence of  $\sim 2-3$  mag optical eclipses in light curves spanning  $\lesssim 2$  hr. In addition, most will be members of the WZ Sge-class (see Kato 2015) and, thus, can also be flagged by the blue excess associated to the dominant white dwarf spectrum. We note in passing that such eclipsing CVs will be of great scientific value in their own right, in particular for computing accurate white dwarf masses and evolutionary studies (e.g. Littlefair et al. 2008).

## 2.5 Other possible outliers

While high-inclination short-period CVs represent our main concern, some contamination may also be expected from other stellar populations. For example, broad molecular bands in late M-type stars (see Figure 8) and S-type symbiotic binaries (Munari & Zwitter 2002) can mimic very broad  $\text{H}\alpha$  emission lines with  $\text{FWHM}\approx 5400 \text{ km s}^{-1}$ . These could be confused with extreme BHs but are readily spotted by their extreme red colours in optical/NIR broadband photometry.

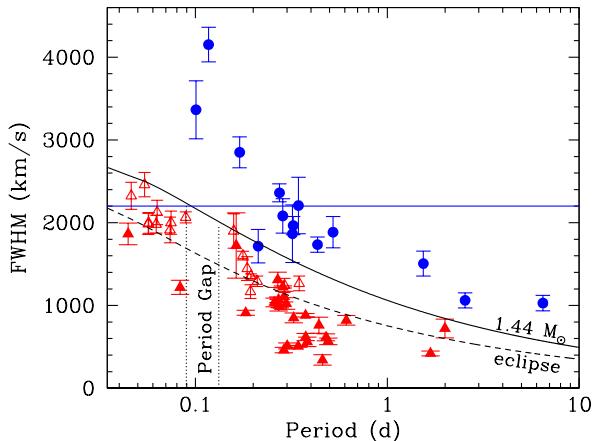


**Figure 9.** FWHM versus  $P_{\text{orb}}$  for a sample of BH XRTs (filled blue circles) and CVs (red triangles). Eclipsing CVs are indicated by open red triangles. The black solid line indicates a hard upper limit in FWHM for CVs, set by the Chandrasekhar mass, while the black dashed line represents a lower limit for eclipsing CVs. The blue horizontal line marks our FWHM cut-off and the vertical dotted lines the edges of the period gap for CVs. Only eclipsing CVs with orbital periods under the gap can produce  $H\alpha$  lines with  $\text{FWHM} > 2200 \text{ km s}^{-1}$ .

D-type symbiotics, on the other hand, pose no hazard as their nebular-type spectra typically have very large EWs  $\gtrsim 1000 \text{ \AA}$ .

A small fraction of WN-type Wolf-Rayet stars (Smith et al. 1996) can certainly produce very broad emission lines ( $H\alpha$ , He I, He II) within the spectral band covered by our narrow-band filters but they are very scarce and tightly confined to star forming clusters, not to be targeted by our proposed survey (see Section 3.1). Likewise, QSOs and AGNs (Seyfert 1s) at specific redshifts can bring broad emission lines into our photometric band. Contamination from  $H\alpha$  and N III  $\lambda 6548$  will be produced at  $z < 0.01$  although these nearby AGNs are a trifle and will be immediately recognized as extended (non-stellar) objects. Further contamination from  $H\beta$ ,  $H\gamma$ , Mg II  $\lambda 2798$ , C III  $\lambda 1909$ , C IV  $\lambda 1459$  and  $\text{Ly}\alpha$  is expected at redshifts  $z=0.34\text{--}0.36$ ,  $0.50\text{--}0.52$ ,  $1.33\text{--}1.36$ ,  $2.41\text{--}2.47$ ,  $3.44\text{--}3.56$  and  $4.3\text{--}4.5$ , respectively. Scaling from the 13th edition of the Veron Catalogue of QSO & AGNs (Véron-Cetty & Véron 2010) we estimate an incidence of  $\sim 0.5 \text{ deg}^{-2}$  (66% from Mg II and C III) for magnitudes  $V \leq 22$ . However, given the observed distribution of line widths (Puchnarewicz et al. 1997) only about  $\sim 43\%$  are expected to possess  $\text{FWHM}=2200\text{--}5400 \text{ km s}^{-1}$  and, therefore, the density of AGNs/QSOs is effectively cut down to  $\sim 0.23 \text{ deg}^{-2}$ . In any case, contaminating AGNs/QSOs can be further isolated through the lack of short timescale variability and mid-IR colour cuts (Mateos et al. 2012; Stern et al. 2012, 2015). Finally, ultracompact AM CVn binaries (Solheim 2010), despite the lack of  $H\alpha$  lines, possess strong broad He I  $\lambda 6678$  emission which results in fake EWs through equation 3. Fortunately, AM CVns are invariably placed in the  $H\alpha$  colour diagram under the focus point (i.e.  $\text{EW} < 0$ ) as proved by synthetic colours obtained from seven Sloan AM CVn stars.

A final word of caution must be said on our photometric system. Equation 4 has been calibrated assuming simulated double-peaked profiles which adequately describe quiescent BH lines (Appendix A). If real emission lines have different shapes then  $\text{FWHM}_{\text{ph}}$  values may deviate with respect to true FWHMs by a few hundred  $\text{km s}^{-1}$ . In particular, we find that FWHMs can be overestimated by  $\sim 200 \text{ km s}^{-1}$  in a composite profile with a broad base and narrow peak (i.e. typical of novalikes and magnetic CVs). On the other hand, in case of double-peaked emission superposed on broad absorption features (characteristic of some high-inclination WZ Sge stars) FWHMs are underestimated by a similar amount. In any case, we note that none of these represent a problem here because FWHMs in novalike/magnetic CVs never surpass our width cut-off while, for the latter case, the bias goes in the direction of increasing the number of rejections.

It should also be stressed that, because our photometric system is biased towards selecting stars with broad  $H\alpha$  emission lines it will not find potential BHs with intermediate ( $\approx 2\text{--}5 M_{\odot}$ ) nor massive ( $\gtrsim 10 M_{\odot}$ ) companion stars. However, the contribution of these to the population of BH X-ray binaries is likely to be small, as indicated by both population synthesis simulations (e.g. Kalogera 1999; Grudzinska et al. 2015) and observations: only three BHs with intermediate mass donors have been found among the sample of  $\sim 60$  XRTs (Corral-Santana et al. 2016) while two BHs with massive companions (Cyg X-1 and MWC 656, Casares et al. 2014) are known in the Galaxy.

### 3 HAWKS: A SURVEY TO DISCOVER HIBERNATING BLACK HOLES

Thus far, we have shown that quiescent BH XRBs can be efficiently selected using photometric techniques, provided that a cut-off at  $\text{FWHM} \geq 2200 \text{ km s}^{-1}$  is set for the width of the  $H\alpha$  emission. In what follows, we describe a survey strategy specifically designed to discover new quiescent BHs by exploiting the photometric system hitherto discussed.

#### 3.1 Scientific requirements and survey strategy

The so-called *HAlpha-Width Kilo-deg Survey* (HAWKs hereafter) hinges upon two scientific requirements. Firstly, we aim to measure  $\text{FWHM}_{\text{ph}}$  at  $\approx 10\%$  accuracy to match the intrinsic FWHM variability observed in quiescent BH XRTs (see Paper I). And secondly, the effective width of the  $H\alpha_n$  filter (which sets the spectral resolution of the photometric system) should be lower than our width cut-off. In order to ensure a clean identification of candidates we define the width of the  $H\alpha_n$  filter to be  $1700 \text{ km s}^{-1}$  or  $37 \text{ \AA}$ . This is motivated by the fact that the bulk of contaminants are narrow  $H\alpha$  emitters that will cluster at the  $H\alpha_n$  width limit in the  $H\alpha$  colour diagram. Therefore, given a 10% precision in FWHM measurements, our choice of  $H\alpha_n$  width implies that the great majority of contaminants will be placed under the  $2200 \text{ km s}^{-1}$  cut-off with  $3\text{-}\sigma$  confidence and, thus, can be easily rejected.

The two previous requirements put strong constraints on photometric accuracy. In order to estimate the signal-to-noise (S/N) required to achieve a 10% fractional error in FWHM with the  $37 \text{ \AA}$   $H\alpha_n$  filter we decided to perform a



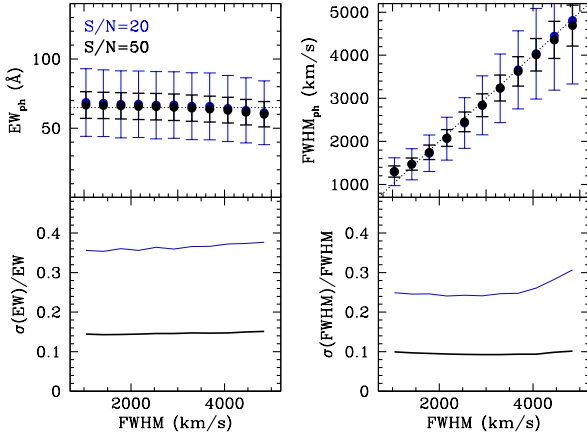


**Figure 10.** Photometric EWs (left) and FWHMs (right) as measured from Monte-Carlo simulations of  $10^4$  synthetic spectra with added noise. The simulated spectra have  $EW=65 \text{ \AA}$  and FWHM in the range  $1000\text{--}5000 \text{ km s}^{-1}$ . Two examples are shown for  $S/N=20$  (thin blue line) and  $S/N=50$  (thick black line), as measured by our three photometric filters. Filled circles and errorbars indicate the mean and  $\pm 1\text{-}\sigma$  confidence level in the PDF distributions. The bottom panels display the fractional error in EW (left) and FWHM (right) for the two  $S/N$  cases.

Monte-Carlo analysis with  $10^4$  trials. Poissonian noise was injected to a grid of synthetic BH spectra, with EWs in the range  $10\text{--}200 \text{ \AA}$  and FWHMs between  $1000\text{--}5000 \text{ km s}^{-1}$ . Simulated fluxes were then computed by convolution with the filter’s response and used as inputs to equations 3 and 4 to produce the PDFs of  $EW_{\text{ph}}$  and  $FWHM_{\text{ph}}$ . Since the outcome is totally dominated by the narrowband filter,  $H\alpha_n$ , we impose the additional condition that the  $S/N$  on the two other filters must be equal to the one for  $H\alpha_n$ . It should be noted that relaxing this demand does neither lead to a significant improvement in  $S/N$  nor survey speed. Figure 10 presents the results of the Monte-Carlo simulation for the case of an  $H\alpha$  line with  $EW=65 \text{ \AA}$  and  $S/N=20$  and  $50$ . The choice of  $EW$  is motivated by the mean in the distribution of EWs for the current sample of dynamical BHs. The figure shows that  $S/N \geq 50$  is needed to measure FWHMs to better than 10% for this specific  $EW$ . Obviously, the  $S/N$  limit increases at lower EWs (for example,  $S/N \geq 60$  for  $EW \leq 50 \text{ \AA}$ ), but in what follows, we take this result as representative of the BH population and propose  $S/N=50$  as the goal of the HAWKs survey.

Quiescent BH XRTs are known to exhibit significant flickering, both in the continuum and  $H\alpha$  flux, which can be an issue of concern (Hynes et al. 2002; Zurita et al. 2003; Shahbaz et al. 2004). Because flickering displays on characteristic time scales of  $\approx \text{min}$  it can be averaged out if photometric observations are split into short individual blocks. For instance, single  $S/N=50$  exposures can be divided into  $10 r/H\alpha_b/H\alpha_n$  cycles of  $S/N \sim 16$  per filter, thereby minimizing the impact of flickering variability on FWHM determinations. This strategy has the additional advantage of extending the dynamic range, avoiding the saturation of relatively bright stars.

HAWKs will focus on the Galactic Plane because 90%

of the  $\sim 60$  BH transients detected so far lie in the disc at  $|b| < 10^\circ$  (Corral-Santana et al. 2016). The survey should preferentially target selected sky fields with low IS extinction to maximize the surveyed volume. Inspection of radial extinction profiles from 2MASS (Marshall et al. 2006) and IPHAS (Sale et al. 2014) reveal some low extinction windows close to the Galactic Plane. For example, sightlines along  $l \approx 55\text{--}75^\circ$  above the Plane probe the inter-arm region between the Perseus and Sagittarius arms to considerable depths. This area will be hereafter referred to as *Window 1* (W1). Other expedient sightlines are identified below the Galactic Plane at  $l \approx 40\text{--}60^\circ$  (W2),  $l \approx 85\text{--}110^\circ$  (W3) and  $l \approx 115\text{--}140^\circ$  (W4) (similar low extinction windows are reachable in the southern Galactic Plane). We find that these sightlines typically have  $A_r \lesssim 2.4$  up to  $\approx 6 \text{ kpc}$  ( $0.4 \text{ mag/kpc}$ ), even at low latitudes  $b \sim 2^\circ$  (see Figure 11).

A dedicated survey of these fields would produce a catalogue of hibernating BH candidates with broad  $FWHM > 2200 \text{ km s}^{-1} H\alpha$  emission. In Section 2.4 we showed that significant contamination is expected from AGNs and high inclination CVs with  $P_{\text{orb}} < 2.1 \text{ h}$ . Therefore, intensive photometric monitoring of candidates will need to be programmed in 2 h time slots (for instance using a robotic facility) to detect eclipsing CVs and steady (non-variable) AGNs. A very efficient way to identify AGNs is also through mid-IR colours: as opposed to single stars, XRBs or CVs, AGNs are strong mid-IR emitters which can be efficiently selected using appropriate colour cuts based upon *WISE* or *Spitzer* bands (see e.g. Mateos et al. 2012; Stern et al. 2015). Finally, the remaining BH candidates can be confirmed through photometric mass functions (Equation 2), which requires a knowledge of their orbital periods. This can be secured from further photometric monitoring, using specific cadence strategies optimized for period detection in the range 2 h - 1 d. Here the upper bound is set by the maximum  $P_{\text{orb}}$  for an extreme  $15 M_\odot$  BH (see e.g. Fryer & Kalogera 2001, also Belczynski et al. 2010) to produce  $FWHM > 2200 \text{ km s}^{-1}$ . The final output of the HAWKs survey will thus be a list of confirmed BHs with  $PMF \geq 3 M_\odot$ .

### 3.2 The hibernating BH population

A key question to follow is how many quiescent BHs can be discovered by HAWKs and this depends primarily on the size of the hibernating population. To address this issue we first look at empirical estimates. Modern extrapolations of the number of X-ray transients detected thus far suggest a Galactic population of  $\approx 2000$  dormant BHs (Romani 1998; Corral-Santana et al. 2016). These estimates, however, are most likely biased low because of survey incompleteness and a number of complex selection effects. For example, arguments have been presented for the existence of a hidden population of BHs with cold globally stable discs and, thus, suppressed outburst activity (Menou et al. 1999). Furthermore, it has been shown that BH XRTs with short orbital periods  $\lesssim 4 \text{ h}$  may be concealed because of low peak X-ray outburst luminosities (Wu et al. 2010; Kneivitt et al. 2014). Also, the paucity of dynamical BHs with orbital inclinations  $> 75^\circ$  strongly indicates that high inclination BHs are X-ray obscured by their accretion discs and thus difficult to detect (Narayan & McClintock 2005, see also Corral-Santana

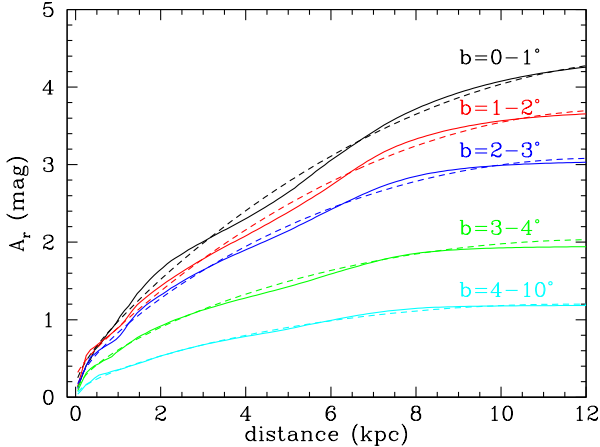


**Figure 11.** Average radial extinction profiles for window W1 ( $l = 55 - 75^\circ$ ) and five latitude bands. Dashed lines indicate the best fitting curves to each profile.

et al. 2013). Considering this we believe the observational projections are underestimated by a factor of a few.

Standard binary population models, on the other hand, have problems reproducing the empirical numbers because of the energetics of the Common Envelope (CE) phase. It is exceedingly difficult for the low-mass companion to eject the envelope of the massive star and most progenitor binaries are predicted to end up in mergers (see e.g. Portegies Zwart et al. 1997). Other simulations involving less standard CE parameters or alternative formation paths do, however, predict  $10^3 - 10^4$  BHs in the Galaxy, in better agreement with observations (see review in Li 2015). Given the above, we here decide to adopt a Galactic population of 5000 hibernating BHs.

### 3.3 Estimated number of BHs to be revealed by HAWKs

Armed with the census of hibernating BHs we can now provide an estimate of the number to be discovered by HAWKs. Here we assume that the density of BHs follows an exponential distribution

$$\rho = \rho_0 \exp(-z/h) \quad (6)$$

with  $z$  being the distance perpendicular to the Galactic Plane and  $h$  the scale height. We start by adopting  $h \sim 0.167$  kpc, consistent with the scale height of stars in the thin disc (Binney & Tremaine 2008). The normalization for a population of 5000 BHs thus implies a Galactic mid-plane density  $\rho_0 = 24 \text{ kpc}^{-3}$ . A crucial aspect in this calculation is the radial distribution of interstellar extinction along our proposed sightlines. As an example, we have examined IPHAS extinction profiles for sky region W1.

Radial profiles were downloaded from Sale et al. (2014) (<http://www.iphas.org/extinction/>) for six latitude bands between  $b = 0^\circ$  and  $5^\circ$  and these have been averaged within the longitude interval of W1 to produce a mean extinction profile per latitude band. IPHAS provides  $A_0$ , the monochromatic extinction at  $5495 \text{ \AA}$ , and, therefore,

**Table 1.** Maximum probed distance and number of BHs in window W1 for scale height  $h = 0.167$  kpc and three survey magnitudes

| b                    | r=21    |            | r=22    |            | r=23    |            |
|----------------------|---------|------------|---------|------------|---------|------------|
|                      | d (kpc) | Number BHs | d (kpc) | Number BHs | d (kpc) | Number BHs |
| $0^\circ - 1^\circ$  | 3.6     | 2.0        | 4.7     | 4.3        | 6.0     | 8.5        |
| $1^\circ - 2^\circ$  | 3.8     | 1.7        | 5.0     | 3.5        | 6.6     | 6.7        |
| $2^\circ - 3^\circ$  | 4.1     | 1.6        | 5.5     | 2.9        | 7.4     | 5.1        |
| $3^\circ - 4^\circ$  | 5.0     | 1.7        | 7.1     | 2.9        | 10.2    | 4.4        |
| $4^\circ - 10^\circ$ | 6.3     | 4.6        | 9.4     | 6.0        | 15.3    | 6.6        |
| TOTAL BHs            | -       | 12         | -       | 20         | -       | 31         |

these values were converted into r-band extinction through  $A_r = 0.748 A_0$  (Cardelli, Clayton & Mathis 1989). We find that the extinction profiles can be modeled with a combination of a quadratic and power functions following  $A_r(d) = a_0 d \times (1 + a_1 d) + a_2 d^{a_3}$ , with  $d$  being the distance along a given sightline and  $a_0 - a_3$  the fitting coefficients. Figure 11 displays the average radial extinction profiles together with the best model fits for our five representative latitude slices. Here, because IPHAS extinction maps are constrained to  $|b| < 5^\circ$ , we have taken the conservative approach of extending the profile of slice  $b = 4^\circ - 5^\circ$  to the entire latitude strip  $b = 4^\circ - 10^\circ$ .

The maximum surveyed distance for a given sightline is provided by the distance modulus equation

$$\left( \frac{d}{\text{kpc}} \right) = 10^{[0.2(m_r - M_r - A_r(d)) - 2]} \quad (7)$$

where we adopt the absolute magnitude of the prototypical binary A0620-00 ( $M_r = 6$ ) as representative of the BH XRT population. The total number of BHs will thus be obtained by integrating equation 6 over window W1, subdivided into five latitude bands (i.e.  $b = 0^\circ - 1^\circ$ ,  $1^\circ - 2^\circ$ ,  $2^\circ - 3^\circ$ ,  $3^\circ - 4^\circ$  and  $4^\circ - 10^\circ$ ), and to a depth given by equation 7. Table 1 lists the total number of BHs in field W1 for three different survey magnitudes. It also provides a breakdown of the number of BHs per latitude slice.

It should be noted, however, that the numbers given in Table 1 are likely to be conservative for several reasons. First, we have assumed that BH XRTs follow the scale height of the thin disc whilst recent studies support a larger value  $h \approx 0.69$  kpc, consistent with the presence of significant BH kick velocities (Repetto et al. 2017). Remarkably, while the scale height does not affect the number of BHs at  $r=21$ , it does have a significant impact at higher depths, with a 30% increase for  $r=22$  (and a factor two for  $r=23$ ). This is reflected in Table 2 where we list the number of BHs for  $h = 0.69$  kpc and three survey magnitudes<sup>4</sup>. In this regard, it is interesting to note that a direct comparison of the number of BHs per latitude band with binary population simulations can readily demonstrate the existence of high natal kicks during BH formation (Jonker & Nelemans 2004; Repetto et al. 2012, 2017). As we see in Tables 1 and 2, this is achievable

<sup>4</sup> A mid-plane density  $\rho_0 = 6 \text{ Kpc}^{-3}$  has been adopted here so that the total number of BHs is 5000.

**Table 2.** Number of BHs in window W1 for scale height  $h = 0.69$  kpc and three survey magnitudes

| b         | r=21<br>Number<br>BHs | r=22<br>Number<br>BHs | r=23<br>Number<br>BHs |
|-----------|-----------------------|-----------------------|-----------------------|
| 0° – 1°   | 0.6                   | 1.2                   | 2.5                   |
| 1° – 2°   | 0.6                   | 1.3                   | 2.9                   |
| 2° – 3°   | 0.7                   | 1.6                   | 3.5                   |
| 3° – 4°   | 1.1                   | 2.8                   | 6.7                   |
| 4° – 10°  | 8.3                   | 19.0                  | 44.3                  |
| TOTAL BHs | 11                    | 26                    | 60                    |

with a single 200 sqr deg field, such as W1, down to a depth  $r \sim 22$ .

And secondly, because of the lack of accurate extinction profiles for latitudes  $b > 5^\circ$  we have extended the IPHAS profile for  $b = 4 - 5^\circ$  to  $b = 4^\circ - 10^\circ$ . If we take instead a typical (but less accurate) NIR extinction profile for ( $l = 65^\circ$ ,  $b = 7.5^\circ$ ) as given in Marshall et al. (2006) and convert it into r-band extinction through  $A_r = 6.68A_K$  (Cardelli, Clayton & Mathis 1989), we find that the number of BHs is further boosted (e.g.  $\approx 41$  for  $r=22$ ). On the other hand, we should bear in mind that, as shown in Section 2.3, our  $FWHM \geq 2200 \text{ km s}^{-1}$  cut-off will select  $\sim 46\%$  of the BH population contained in a given survey volume and, therefore, HAWKS would only be able to detect half of the numbers listed in Table 2.

To conclude this Section we look at the number of outliers expected for window W1. In the case of CVs we assume an exponential density profile in the vertical direction with  $\rho_0 = 2 \times 10^4 \text{ kpc}^{-3}$  (Politano 1996; Pretorius & Knigge 2012; Burenin et al. 2016) and  $h = 0.26$  kpc, appropriate for the disc scale height of old, short period CVs (Pretorius et al. 2007). Following Warner (1987) we adopt an absolute magnitude  $M_V = 9$ , characteristic of short period CVs, and a typical quiescent colour ( $V - R$ )  $\approx 0$ . Integrating equation 6 over window W1 yields 4600 CVs for a survey depth  $r=22$ . But, since only 0.1% will possess  $FWHM > 2200 \text{ km s}^{-1}$  (Section 2.3) we expect to select  $\approx 5$  CVs. Regarding AGNs, in Section 2.5 we predicted  $\approx 0.23$  per sqr deg for  $V < 22$  which results in  $\approx 46$  AGNs for window W1. We note, however, that this is an upper limit because it neglects Galactic absorption which can amount to several magnitudes in the Plane. Adopting the extinction profiles derived in Figure 11 for W1 and using statistics from the Veron Catalogue we estimate that our sample will contain  $\approx 38$  AGNs.

In summary, for a survey magnitude  $r=22$  and a BH scale height  $h \sim 0.69$  kpc we predict HAWKS will select  $\approx 56$  candidates with  $FWHM > 2200 \text{ km s}^{-1}$  in 200 sqr deg. These will include  $\approx 5$  CVs,  $\approx 38$  AGNs and  $\approx 13$  hibernating BHs which can be singled out through photometric variability. Contaminating AGNs can also be detected and weed out through mid-IR colours. A survey of 800 sqr deg would therefore produce  $\approx 50$  new dynamical BHs i.e. a three-fold improvement over the currently known sample.

## 4 DISCUSSION

BH XRTs are presently discovered at a rate of  $\sim 1.7 \text{ yr}^{-1}$  but less than a third remain sufficiently bright in quiescence for radial velocity analysis. As a result, after 50 years of careful scrutiny of the X-ray sky only 17 BHs have been dynamically confirmed and, therefore, about a century seems necessary to simply double the number. A prime goal in the field would thus be to unveil a large homogeneous sample of secure (dynamical) quiescent BHs. To this end we have presented a novel approach to uncover an unprecedented large sample of dormant BHs. This can be achieved through a deep ( $r \sim 22$ ) survey using a combination of carefully chosen H $\alpha$  filters. The filters are specially customized to resolve H $\alpha$  widths  $FWHM > 2200 \text{ km s}^{-1}$ , a limit which, as we showed in Section 2.5, would allow selecting  $\sim 46\%$  of the hidden BH population while filtering out the vast majority of contaminants. Furthermore, the combination of H $\alpha$  widths with orbital information (supplemented by photometric follow-up of candidates), will lead to *photometric* mass functions and thus dynamical confirmation of hibernating BHs.

The new concept presented in this paper (i.e. photometric BH selection) opens the door to weigh BHs through imaging and, thus, search for BHs in large volumes to unprecedented depths, a potential breakthrough in the field. We estimate that  $\approx 13$  BHs can be unveiled in an area of 200 sqr deg and, therefore, a survey organized around this technique can lead to an order of magnitude improvement on dynamical BH statistics in just a few years. This would allow constraining, not only the space properties of the population (i.e. Galactic Plane density, scale height and total number) but also the distribution of orbital periods and, ultimately, the BH mass spectrum. These three observables encode key information on BH formation and evolution. For example, the total number of BHs is very sensitive to binary evolution parameters such as the efficiency of common envelope ejection, mass-loss rate of He stars or the survival rate after supernova explosion (e.g. Kalogera 1999; Podsiadlowski, Rappaport & Han 2003; Kiel & Hurley 2006). Meanwhile, the observed scale height is driven by the presence of natal kicks, a current hot topic in the field (Jonker & Nelemans 2004; Fragos et al. 2009; Repetto et al. 2017; Mirabel 2017; Casares, Jonker & Israelian 2017). It should be stressed here that, even if the total number of discovered BHs turns out to be lower than predicted, HAWKS will still set stringent constraints on BH formation models.

On the other hand, the BH mass spectrum strongly depends on poorly constrained supernova physics, starting with the nature of the explosion mechanism itself (Fryer et al. 2012; Ugliano et al. 2012; Kochanek 2014). An expanded sample will, for instance, allow quantification of the significance of the gap in the mass distribution (Özel et al. 2010; Farr et al. 2011; Kreidberg et al. 2012) or test the claimed BH mass-period relation (Lee, Brown & Wijers 2002). The latter was proposed to stem from a correlation with BH spin and thus, if true, it should be closely connected to the production of long-duration gamma-ray bursts. It should also be noted that, because HAWKS is biased towards H $\alpha$  emitters, BH X-ray binaries with hotter early-type companions will be missed. However, as mentioned earlier, both population synthesis models and current observations strongly

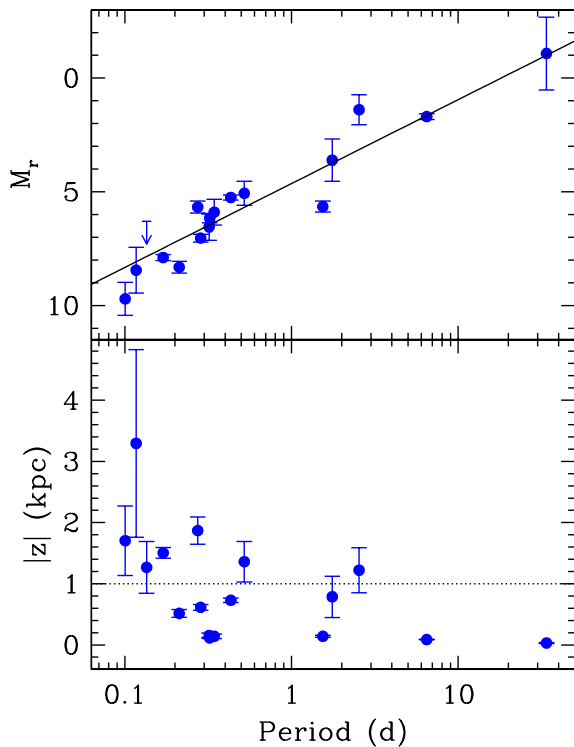


**Figure 12.** Top: Absolute magnitudes of quiescent BH XRTs with low-mass companion stars as a function of orbital period. The best least squares fit is overlotted. Bottom: Vertical elevation above the Galactic plane versus orbital period. The dotted horizontal line marks the limit of the Galactic thin disc.

suggest that the impact of the latter on the distribution of BH masses is likely to be negligible.

Finally, the orbital period distribution is shaped by the length of time BH X-ray binaries spend in a given period bin and, therefore, on the relative importance of gravitational radiation versus magnetic braking (Knigge et al. 2011), with perhaps other unknown angular momentum loss mechanisms also playing a role, as suggested by recent observations of fast orbital period decays (González Hernández, Rebolo & Casares 2014). As an example, the elusive minimum period spike predicted by CV evolution models was a subject of debate for decades until a faint population of quiescent CVs was revealed by SLOAN (Gänsicke et al. 2009). Similarly, the outcome of the HAWKs survey will allow for constraints on the lower limit in the hibernating BH period distribution, searching for evidence of a gap and a possible accumulation of systems around a minimum period.

The study of BH XRTs with short orbital periods has strategic interest because these might represent a large fraction of the whole hibernating population, with different bulk properties than the existing sample. To illustrate this, we have compiled in Table 4 quiescent properties of the known BH XRTs with low-mass companion stars. Two binaries (GRS1915+105 and GX 339-4) have not yet returned to quiescence after discovery and, thus, we decided to adopt their deepest optical magnitudes reported to date, which

correspond to epochs of minimum X-ray activity. Because of their long orbital periods and luminous companion stars, we expect irradiation effects to be negligible at these low levels. Therefore, we tentatively adopt these magnitudes as representative of their true quiescent luminosity. In any case, it should be noted that the error in absolute magnitude for these two sources is dominated by uncertainties in the distance and, in the case of GRS1915+105, also reddening.

Figure 12 displays the evolution of absolute magnitude ( $M_r$ ) and elevation above the Galactic plane ( $z$ ) as a function of orbital period. Interestingly, we observe that  $M_r$  is tightly correlated with orbital period across 10 magnitudes (i.e. 4 decades in luminosity), with a correlation coefficient -0.95. A least squares fit yields

$$M_r = 4.64(0.10) - 3.69(0.16) \log P_{\text{orb}} (d), \quad (8)$$

a relation which, in turn, may prove useful to infer distances to BH XRTs when the orbital period is known. The mean absolute magnitude for the period interval 2-4 h is  $M_r \approx 9$ , i.e. 3 magnitudes fainter than that of BH XRTs at the peak of the period distribution. This makes short period BHs difficult to detect by HAWKs unless the search is pushed to deeper limits  $r \sim 24$ . On the other hand, the bottom panel in Figure 12 shows that short period BHs tend to be located in the Galactic thick disk at  $z \geq 1$  kpc and, consequently, are less affected by interstellar absorption. Although this may be a selection effect (short period binaries might be X-ray dimmer and, therefore, more heavily obscured in the plane) it implies that short period BHs are best targeted at higher Galactic latitudes. At  $S/N \sim 15$  for  $r \sim 24$  HAWKs should still be able to identify short period BHs, given their typically large  $\text{FWHM} \approx 3000\text{-}4000 \text{ km s}^{-1}$  (see Figure 9), or, at least, put useful constraints on their abundance.

It should also be mentioned that HAWKs is sensitive to the discovery of massive (high inclination) NSs in XRBs and Redbacks in the disc state, the evolutionary link between Low Mass X-ray Binaries and recycled millisecond pulsars (Roberts 2013). The construction of the mass distribution of NSs is one of the fundamental experiments in high energy astrophysics from which new light on the composition of ultradense matter can be shed (Özel & Freire 2016). In addition, as shown by Figure 8, the  $H\alpha$  colour diagram is very efficient at discriminating  $H\alpha$  emitting objects from normal stars. The survey will thus render a flux-limited sample of other populations of  $H\alpha$  emitters down to unprecedented depths which will allow a plethora of ancillary studies. In particular it will greatly expand the number of WZ Sge stars with secure periods below the gap, a key sample to constrain formation and evolutionary channels in CVs. This sample will likely contain massive accreting white dwarfs, which will make excellent candidates for Type Ia supernova precursors (Littlefair et al. 2008; Maoz, Mannucci & Nelemans 2014). As a matter of fact, new generation synoptic surveys (e.g. the *Large Synoptic Survey Telescope LSST*, Abell et al. 2009) and wide-field multi-object spectrographs (e.g. WEAVE, Dalton et al. 2012) will secure optical colours, variability information and classification spectra of interesting subsets of  $H\alpha$  emitters selected from HAWKs. For example routine light curves and spectra of sources with  $\text{FWHM}_{\text{ph}} > 1800 \text{ km s}^{-1}$  will likely reveal large numbers of eclipsing white dwarfs and NS binaries, (ideal for accurate



mass determinations) plus many more BHs, a factor  $\sim 1.8$  larger than hitherto quoted.

## 5 CONCLUSIONS

We have presented HAWKs, a photometric survey with custom  $H\alpha$  filters designed for the efficient detection of dormant BHs in large fields of view to unprecedented depth. The main conclusions of the paper are as follows:

- FWHMs of  $H\alpha$  emitting stars can be recovered from photometric observations using a combination of r-band continuum filter and two  $H\alpha$  filters (one broad and another narrow), all centered at the rest wavelength of  $H\alpha$ . We define a photometric system based on these three filters and show how  $H\alpha$  emitters can be effectively separated from normal stars in a colour-colour diagram, independently of their SEDs and interstellar reddening.

- We find that a width cut-off at  $\text{FWHM} > 2200 \text{ km s}^{-1}$  allows the selection of  $\sim 46\%$  of hibernating BHs while filtering out the great majority of  $H\alpha$  emitters. Only AGNs at particular redshift bands and a small number of eclipsing short period CVs can contaminate the sample. Fortunately, these are easily flagged from variability properties in 2 h light curves, with AGNs being steady sources while CVs display deep eclipses. AGNs can also be identified from mid-IR colour cuts.

- BH candidates selected by our photometric system will be dynamically confirmed through *Photometric Mass Functions*. These are obtained by combining the photometric FWHMs with orbital period information derived through photometric variability. This strategy establishes the basis for HAWKs, an *HAlpha-Width Kilo-deg* Survey of the Galactic plane.

- We predict HAWKs will discover  $\approx 13$  hibernating BHs in a survey of 200 sqr deg at depth  $r=22$ . This calculation assumes a Galactic population of  $\sim 5000$  dormant BHs, distributed with a scale height  $h=0.69 \text{ kpc}$  and similar properties as the currently known sample i.e. same distribution of quiescent luminosities, orbital periods and BH masses. Based on these numbers we expect an order of magnitude improvement in the statistics of dynamical BHs through a survey area of  $\approx 1 \text{ kilo sqr deg}$ , a goal which is achievable in only a few years.

- The previous estimates are, however, subject to considerable uncertainty due to possible unknown biases affecting the existing sample. In any event, only through a deep specialized survey such as HAWKs is it possible to constrain the size and properties of the hidden BH population. For example, both the scale height and population size are very sensitive to the number of BHs detected at Galactic latitudes  $b \sim 5^\circ - 10^\circ$  and depths  $r \sim 22 - 23$ . These parameters could be constrained from a limited survey area of  $\sim 200 \text{ sqr deg}$ , such as the one proposed for W1. We believe the outcome of HAWKs may revolutionize the study of stellar-mass BHs by significantly boosting the census, setting stringent constraints on the properties of the population and paving the way for demographic studies.

## ACKNOWLEDGEMENTS

This work was supported by the Leverhulme Trust through the Visiting Professorship Grant VP2-2015-046. Also by the Spanish Ministry of Economy, Industry and Competitiveness (MINECO) under the 2015 Severo Ochoa Program MINECO SEV-2015-0548. We would like to acknowledge the hospitality of the Department of Physics of the University of Oxford, where this work was performed during a sabbatical visit. The author is also grateful to Mansfield College for the support provided by a Visiting Fellowship and the kindness of its staff. We thank P.A. Charles, R. Fender, T. Maccarone, T. Muñoz-Darias, M.A.P. Torres, P. Ghandi and J.A. Fernández-Ontiveros for many interesting discussions and comments to the manuscript. We also thank the anonymous referee for helpful suggestions that have improved the quality of the paper.

**Table 3.** Population fraction selected as a function of FWHM cut-off values.

| Model<br>Population | FWHM<br>> 1000 km s <sup>-1</sup> | FWHM<br>> 1500 km s <sup>-1</sup> | FWHM<br>> 1800 km s <sup>-1</sup> | FWHM<br>> 2000 km s <sup>-1</sup> | FWHM<br>> 2200 km s <sup>-1</sup> | FWHM<br>> 2400 km s <sup>-1</sup> | FWHM<br>> 2600 km s <sup>-1</sup> |
|---------------------|-----------------------------------|-----------------------------------|-----------------------------------|-----------------------------------|-----------------------------------|-----------------------------------|-----------------------------------|
| CV-1                | 0.931                             | 0.505                             | 0.136                             | 0.016                             | $3 \times 10^{-4}$                | 0                                 | 0                                 |
| CV-2                | 0.996                             | 0.769                             | 0.224                             | 0.038                             | 0.001                             | $1 \times 10^{-4}$                | $4 \times 10^{-5}$                |
| BH                  | 0.999                             | 0.965                             | 0.811                             | 0.633                             | 0.459                             | 0.327                             | 0.238                             |

**Table 4.** Quiescent properties of BH XRTs with low mass companion stars

| Source           | $P_{\text{orb}}$<br>(days) | $d$<br>(kpc) | $m_r$<br>(mag) | $E(B-V)$ | $M_r$<br>(mag) | $b$<br>(deg) | $ z  = d \sin  b $<br>(kpc) |
|------------------|----------------------------|--------------|----------------|----------|----------------|--------------|-----------------------------|
| GRS 1915+105     | 33.85                      | 9.0±2.0      | 28.3           | 6.3±0.5  | -1.08±1.6      | -0.2         | 0.03±0.01                   |
| V404 Cyg         | 6.4713                     | 2.39±0.14    | 16.6           | 1.3      | 1.7±0.1        | -2.1         | 0.09±0.01                   |
| BW Cir           | 2.5445                     | 18-33        | 20.7           | 1.0      | 1.4±0.7        | -2.8         | 1.22±0.37                   |
| GX 339-4         | 1.7557                     | 6-15         | 21.5           | 1.2      | 3.6±0.9        | -4.3         | 0.79±0.34                   |
| XTE J1550-564    | 1.5420                     | 4.5±0.5      | 22             | 1.33     | 5.7±0.2        | -1.8         | 0.14±0.02                   |
| N. Oph 77        | 0.5213                     | 8.6±2.1      | 20.9           | 0.5      | 5.1±0.5        | 9.1          | 1.36±0.33                   |
| N. Mus 91        | 0.4326                     | 5.9±0.3      | 19.8           | 0.3      | 5.3±0.1        | -7.1         | 0.73±0.04                   |
| GS 2000+25       | 0.3441                     | 2.7±0.7      | 21.3           | 1.4      | 5.9±0.6        | -3.0         | 0.14±0.04                   |
| A0620-00         | 0.3230                     | 1.06±0.10    | 17.1           | 0.35     | 6.2±0.2        | -6.2         | 0.11±0.01                   |
| XTE J1650-500    | 0.3205                     | 2.6±0.7      | 22.1           | 1.5      | 6.6±0.6        | -3.4         | 0.15±0.04                   |
| N. Vel 93        | 0.2852                     | 3.8±0.3      | 20.4           | 0.2      | 7.0±0.2        | 9.3          | 0.61±0.05                   |
| XTE J1859+226    | 0.2740                     | 12.5±1.5     | 22.5           | 0.58     | 5.7±0.3        | 8.6          | 1.87±0.22                   |
| GRO J0422+320    | 0.2122                     | 2.5±0.3      | 21.0           | 0.3      | 8.3±0.3        | -11.9        | 0.52±0.06                   |
| XTE J1118+480    | 0.1699                     | 1.7±0.1      | 19.1           | 0.024    | 7.9±0.1        | 62.3         | 1.51±0.09                   |
| Swift J1753-127  | 0.1352                     | 6.0±2.0      | >21            | 0.34     | >6.3           | 12.2         | 1.27±0.42                   |
| Swift J1357-0933 | 0.1170                     | 2.3-6.3      | 21.7           | 0.037    | 8.5±1.0        | 50.0         | 3.29±1.53                   |
| MAXI J1659-152   | 0.1006                     | 6.0±2.0      | 24.2           | 0.26     | 9.7±0.7        | 16.5         | 1.70±0.57                   |

**Notes to table:**  $M_r$  is obtained from the distance modulus equation, assuming average Galactic reddening  $R_V = A_V/E(B-V) = 3.1$  and  $A_r = 0.748 A_V$  (Cardelli, Clayton & Mathis 1989). Remaining values are taken from the BlackCAT catalogue (Corral-Santana et al. 2016) except for:

- **GS 1915+105:**  $m_r$  is derived from  $m_K=13.1$  (minimum X-ray activity; Neil, Bailyn & Cobb 2007), assuming a de-reddened colour  $(m_r-m_K)_0=2.47$ , appropriate for a K5 III (Johnson 1966; Ziolkowski & Zdziarski 2017),  $A_K/A_r = 0.15$  and  $E(B-V)$  from Chapuis & Corbel (2004).
- **BW Cir:**  $d$  from Casares et al. (2009), assuming a 30% uncertainty.
- **GX 339-4:**  $d$  from Hynes et al. (2004) and  $m_r$  from a reported episode of minimum X-ray activity (Lewis, Russell & Shahbaz 2012).
- **Swift J1753-127:**  $d$  from Cadolle Bel et al. (2007).
- **Swift J1357-0933:**  $d$  range constrained from a lower limit in Mata-Sánchez et al. (2015) and an upper limit in Shahbaz et al. (2013).
- **MAXI J1659-152:**  $d$  from Jonker et al. (2012),  $m_r$  from Corral-Santana et al. (2017).

## REFERENCES

- Abbot, B.P. et al. (LIGO Scientific Collaboration and Virgo Collaboration), 2016a, *Phys. Rev. Lett.*, 116, 061102
- Abbot, B.P. et al. (LIGO Scientific Collaboration and Virgo Collaboration), 2016b, *Phys. Rev. Lett.*, 116, 241103
- Abbot, B.P. et al. (LIGO Scientific Collaboration and Virgo Collaboration), 2016, *Phys. Rev. X*, 6, 041015
- Abell, P. A. et al. (LSST Science Collaboration), 2009, *LSST Science Book*, Version 2.0, arXiv:0912.0201
- Belczynski K. et al., 2010, *ApJ*, 714, 1217
- Belczynski K., Holz D.E., Bulik T., O’Shaughnessy R., 2016, *Nature*, 534, 512
- Belloni T.M., Motta S.E., Muñoz-Darias T., 2011, *Bulletin of the Astronomical Society of India*, 39, 409
- Binney J., Tremaine S., 2008, *Galactic Dynamics: Second Edition*. Princeton University Press
- Burenin R.A. et al., 2016, *Astronomy Letters*, 42, 240
- Cadolle Bel M. et al., 2007, *ApJ*, 659, 549
- Cardelli J.A., Clayton G.C., Mathis J.S., 1989, *ApJ*, 345, 245
- Casares J., 2015, *ApJ*, 808, 80 (Paper I)
- Casares J., 2016, *ApJ*, 822, 99 (Paper II)
- Casares J. et al., 2009, *ApJS*, 181, 238
- Casares J., Jonker P.G., 2014, *Space Sci. Rev.*, 183, 223
- Casares J., Negueruela, I., Ribó, M., Ribas I., Paredes J.M., Herero A., Simón-Díaz S., 2014, *Nature*, 505, 378
- Casares J., Jonker P.G., Israelian, G., 2017, *X-ray Binaries in Handbook of Supernovae*, A.W. Alsabti and P. Murdin editors, Springer (arXiv:1701.07450)
- Chapuis C., Corbel S., 2004, *A&A*, 414, 659
- Cholis I., 2017, *JCAP*, 06, 037
- Clesse S., García-Bellido J., 2017, *Physics of the Dark Universe*, 15, 142
- Coleman Miller M., 2016, *Gen. Relativ. Gravit.*, 48, 95
- Corral-Santana J.M., Casares J., Muñoz-Darias T., Rodríguez-Gil P., Shahbaz T., Torres M.A.P., Zurita C., Tyndall A.A., 2013, *Science*, 339, 1048
- Corral-Santana J.M., Casares J., Muñoz-Darias T., Bauer F.E., Martínez-Pais I.G., Russell D.M., 2016, *A&A*, 587, A61
- Corral-Santana J.M. et al., 2017, *MNRAS*, submitted.
- Dalton G. et al., 2012, *Proc. of the SPIE*, 8446, 12
- De Mink S.E., Mandel I., 2016, *MNRAS*, 460, 3545
- Drew J. et al., 2005, *MNRAS*, 362, 753
- Elbert O.D., Bullock J.S., Kaplinghat M., 2017, *MNRAS*, in press (arXiv:1703.02551)
- Farr W.M., Niharika S., Cantrell A., Kreidberg. L., Bailyn C.D., Mandel I., Kalogera V., 2011, *ApJ*, 741, 103
- Fragos T., Willems B., Kalogera V., Ivanova N., Rockefeller G., Fryer C.L., Young P.A., 2009, *ApJ*, 697, 1057
- Fryer C.L., Kalogera V., 2001, *ApJ*, 554, 548
- Fryer C.L., Belczynski K., Wiktorowicz G., Dominik M., Kalogera V., Holz D.E., 2012, *ApJ*, 749, 91
- Gänsicke B.T., 2005, *The Astrophysics of Cataclysmic Variables and Related Objects*, Proc. ASP Conf., 330, 3
- Gänsicke B.T. et al., 2009, *MNRAS*, 397, 217
- González Hernández J.I., Rebolo R., Casares J., 2014, *MNRAS*, 438, L21
- Grudzinska M. et al., 2015, *MNRAS*, 452, 2773
- Howell S.B., Nelson L.A., Rappaport S., 2001, *ApJ*, 550, 897
- Hynes R.I. et al., 2002, *MNRAS*, 330, 1009
- Hynes R.I., Steeghs D., Casares J., Charles P.A., O’Brien K., 2004, *ApJ*, 609, 317
- Jacoby G.H., Hunter D.A., Christian C.A., 1984, *ApJS*, 56, 257
- Johnson H.L., 1966, *ARA&A*, 4, 193
- Jonker P.G., Nelemans G., 2004, *MNRAS*, 354, 355
- Jonker P.G. et al., 2011, *ApJS*, 194, 18
- Jonker P.G., Miller-Jones J.C.A., Homan J., Tomsick J., Fender R.P., Kaaret P., Markoff S., Gallo E., 2012, *MNRAS*, 423, 3308
- Jonker P.G. et al., 2014, *ApJS*, 210, 18
- Jurcevic J.S., Honeycutt R.K., Schlegel E.M., Webbink R.F., 1994, *PASP*, 106, 481
- Kalogera V., 1999, *ApJ*, 521, 723
- Kato T., 2015, *PASJ*, 67, 108
- Kiel P.D., Hurley J.R., 2006, *MNRAS*, 369, 1152
- Kneivitt G., Wynn G.A., Vaughan S., Watson M.G., 2014, *MNRAS*, 437, 3087
- Knigge C., Baraffe I., Patterson J., 2011, *ApJS*, 194, 28
- Kochanek C.S., 2014, *ApJ*, 785, 28
- Kolb U., 1993, *A&A*, 271 149
- Kormendy J., Ho L.C., 2013, *ARA&A*, 51 511
- Kovetz E., Cholis I., Breysse P.C., Kamionkowski M., 2017, *Phys. Rev. D*, 95, 103010
- Kreidberg L., Bailyn C.D., Farr W.M., Kalogera Vicky, 2012, *ApJ*, 757, 36
- Kuulkers E. et al., 2013, *A&A*, 552, A32
- Lee C.-H., Brown G.E., Wijers R.A.M.J., 2002, *ApJ*, 575, 996
- Lewis F., Russell D.M., Shahbaz T., 2012, *ATel* #4162
- Li X.D., 2015, *New Astron. Rev*, 64, 1
- Littlefair S.P., Dhillon V.S., Marsh T.R., Gänsicke B.T., Southworth J., Baraffe I., Watson C.A., Copperwheat C., 2008, *MNRAS*, 388, 1582
- Maoz D., Mannucci F., Nelemans G., 2014, *ARA&A*, 52, 107
- Marshall, D.J., Robin A.C., Reylé C., Schultheis M., Picaud S., 2006, *A&A*, 453, 635
- Marsh T.R., Robinson E.L., Wood J.H., 1994, *MNRAS*, 266, 137
- Mata-Sánchez D., Muñoz-Darias T., R., Casares J., Corral-Santana J.M., Shahbaz T., 2015, *MNRAS*, 454, 2199
- Mateos S. et al., 2012, *MNRAS*, 426, 3271
- Menou K., Narayan R., Lasota, J.-P., 1999, *ApJ*, 513, 811
- Mirabel I.F., 2017, *New Astron. Rev.*, 78, 1
- Munari U., Zwitter T., 2002, *A&A*, 383, 188
- Narayan R., McClintock J.E., 2005, *ApJ*, 623, 1017
- Neil E.T., Bailyn C.D., Cobb B.E., 2007, *ApJ*, 657, 409
- Özel, F., Psaltis D., Narayan R., McClintock J.E., 2010, *ApJ*, 725, 1918
- Özel, F., Freire P., 2016, *ARA&A*, 54, 401
- Paczyński B., 1971, *ARA&A*, 9, 183
- Parker Q.A. et al., 2005, *MNRAS*, 362, 689
- Peterson B.M. et al., 2004, *ApJ*, 613, 682
- Podsiadlowski Ph., Rappaport S., Han Z., 2003, *MNRAS*, 341, 385
- Politano M. , 1996, *ApJ*, 465, 338
- Portegies Zwart S.F., Verbunt F., Ergma E., 1997, *A&A*, 321, 207
- Pretorius M.L., Knigge C., O’Donoghue D., Henry J.P., Gioia I.M., Mullis C.R., 2007, *MNRAS*, 382, 1279
- Pretorius M.L., Knigge C., 2012, *MNRAS*, 419, 1442
- Puchnarewicz E.M. et al., 1997, *MNRAS*, 291, 177
- Repetto S., Davies M.B., Sigurdsson S., 2012, *MNRAS*, 425, 2799
- Repetto S., Igoshev A., Nelemans G., 2017, *MNRAS*, 467, 298
- Ritter H., Kolb U., 2003, *A&A*, 404, 301
- Roberts, M.S.E., 2013, in *IAU Symp. 291, Neutron Stars and Pulsars*, ed. J. van Leeuwen (Cambridge: Cambridge Univ. Press), 127
- Rodríguez C.L., Chatterjee S., Rasio F.A., 2016, *PhRvD*, 93, 084029
- Romani .R.W, 1998, *A&A*, 333, 583
- Sale S.E. et al., 2014, *MNRAS*, 443, 2907
- Sesana A., 2016, *Phys. Rev. Lett.*, 116, 231102
- Shahbaz T. et al., 2004, *MNRAS*, 354, 31
- Shahbaz T., Russell D.M., Zurita C., Casares J., Corral-Santana J.M., Dhillon V.S., Marsh T.R., 2013, *MNRAS*, 434, 2696
- Smith L.F., Shara M.M., Moffat F.J., 1996, *MNRAS*, 281, 163
- Solheim J.-E., 2010, *PASP*, 122, 1133
- Stern D. et al., 2012, *ApJ*, 753, 18
- Stern D. et al., 2015, *ApJ*, 631, 163



- Szkody P. et al., 2011, AJ, 142, 181  
 Torres M.A.P. et al., 2014, MNRAS, 440, 365  
 Ugliano M., Janka H.-T., Marek A., Arcones A., 2012, ApJ, 757, 69  
 Véron-Cetty M.-P., Véron P., 2010, A&A, 518, A10  
 Vestergaard M., Peterson, B.M., 2006, ApJ, 641, 689  
 Wang C., Jia K., Li X.-D., 2016, MNRAS, 457, 1015  
 Warner B., 1973, MNRAS, 162, 189  
 Warner B., 1987, MNRAS, 227, 23  
 Wevers T. et al., 2017, MNRAS, 466, 163  
 Witham A.R., Knigge C., Drew J.E., Greimel R., Steeghs D., Gänsicke B.T., Groot P.J., Mampaso A., 2008, MNRAS, 384, 1277  
 Wu Y.X., YU W., Li T.P., Maccarone T.J., Li X.D., 2010, ApJ, 718, 620  
 Ziółkowski J., Zdziarski A.A., 2017, MNRAS, 469, 3315  
 Zorotovic M., Schreiber M.R., Gänsicke B., 2011, A&A, 536, A42  
 Zurita C., Casares J., Shahbaz T., 2003, ApJ, 582, 369  
 Zurita C., Durant M., Torres M.A.P., Shahbaz T., Casares J., Steeghs D., 2008, ApJ, 681, 1458  
 Zurita C., Corral-Santana J.M., Casares J., 2015, MNRAS, 454, 3351

## APPENDIX A: SYNTHETIC DOUBLE-PEAK PROFILES, FLUXES AND MAGNITUDES

We have created synthetic X-ray binary spectra by adding a symmetric double-peaked  $H\alpha$  profile to a linear continuum of slope  $5 \times 10^{-4}$  ergs  $\text{cm}^{-2}$   $\text{s}^{-1}$   $\text{\AA}^{-1}$ . This particular slope reproduces well the reddened spectra of X-ray binaries such as V404 Cyg, BW Cir or GS 2000+25. The continuum has been normalized to unity at the rest wavelength of  $H\alpha$  ( $\lambda_0 = 6562.76$ ) i.e.

$$f_{\text{cont}} = 0.0005 \times (\lambda - \lambda_0) + 1 \quad (\text{A1})$$

where  $\lambda$  is the wavelength in angstroms. The  $H\alpha$  line profile is modeled as

$$f_{H\alpha} = 0.2 \left( \frac{EW}{\sigma} \right) \times \left( e^{-\frac{(\lambda - \lambda_0 - DP/2)^2}{2\sigma^2}} + e^{-\frac{(\lambda - \lambda_0 + DP/2)^2}{2\sigma^2}} \right) \quad (\text{A2})$$

where  $DP$  stands for the double peak separation of the  $H\alpha$  profile. The area of the profile is set to be the EW of the  $H\alpha$  line. Model profiles were computed for  $DP = 10 - 60$   $\text{\AA}$  and, for practical purposes, we have adopted  $\sigma = DP/3$ .

By definition, the FWHM of the model profile ( $FWHM_m$ ) is equivalent to the double peak separation plus the FWHM of any of the Gaussians that make up the profile i.e.  $FWHM_m = DP + 2\sigma\sqrt{2\ln 2} = 1.785 \times DP$ . On the other hand, it is argued in Paper I that a single Gaussian fit provides a practical and robust determination of the line FWHM for the case of real data. Therefore, a conversion between formal (model) FWHMs and values derived through Gaussian fits ( $FWHM_g$ ) is required. Consequently, we have fitted Gaussian functions to our synthetic profiles and derived  $FWHM_g$  values, which are listed in Table A1 and plotted in figure A1. The quadratic fit

$$FWHM_g = -62.84 + 0.8942 FWHM_m + 5.9 \times 10^{-6} FWHM_m^2 \quad (\text{A3})$$

**Table A1.** Model FWHMs compared to FWHMs from Gaussian fits.

| DP<br>( $\text{\AA}$ ) | Model FWHM<br>( $\text{km s}^{-1}$ ) | FWHM Gaussian<br>( $\text{km s}^{-1}$ ) |
|------------------------|--------------------------------------|---|
| 10                     | 816                                  | 675                                     |
| 15                     | 1224                                 | 1039                                    |
| 20                     | 1632                                 | 1409                                    |
| 25                     | 2040                                 | 1783                                    |
| 30                     | 2448                                 | 2161                                    |
| 35                     | 2856                                 | 2539                                    |
| 40                     | 3264                                 | 2921                                    |
| 45                     | 3672                                 | 3303                                    |
| 50                     | 4080                                 | 3686                                    |
| 55                     | 4488                                 | 4069                                    |
| 60                     | 4896                                 | 4454                                    |

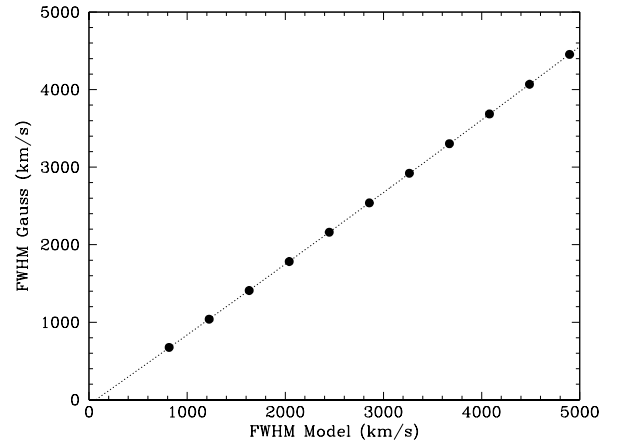


**Figure A1.** FWHMs calculated from a Gaussian fit to synthetic profiles versus model FWHMs. The dotted line depicts the best quadratic fit.

allows obtaining Gaussian FWHMs from formal FWHMs to within 0.6 %.

The flux measured by a given filter is obtained through integrating the synthetic spectra over wavelength, after convolution with the transmission curve of the filter ( $T_{H\alpha_b}$ ), e.g. in the case of filter  $H\alpha_b$

$$F(H\alpha_b) = \int T_{H\alpha_b} \times (f_{\text{cont}} + f_{H\alpha}) d\lambda \quad (\text{A4})$$

Both synthetic spectra and filter response curves are previously sampled to a common bin size of  $1 \text{ \AA pix}^{-1}$ . The fluxes so obtained are subsequently converted into instrumental magnitudes through the expression

$$m_{H\alpha_b} = -2.5 \log F_{H\alpha_b} \quad (\text{A5})$$

and used to construct the  $H\alpha$  colour diagram presented in Section 2.4.

**APPENDIX B: PHOTOMETRIC EW**

We assume a simplified X-ray binary spectrum consisting of a flat continuum and an  $H\alpha$  emission line with square profile. We call  $f_{\text{cont}}$  the continuum flux density level and  $A$  the integrated line flux i.e.  $A = f_{\text{cont}} \times EW$  where  $EW$  stands for the equivalent width of the  $H\alpha$  line. We measure the flux of the X-ray binary using both, a broad r-band and an  $H\alpha$  filter. These filters have equivalent widths  $W_r$  and  $W_{H\alpha_b}$  respectively, with  $W_r > W_{H\alpha_b} > EW$ . For simplicity we also assume the two filters are perfectly squared i.e. Heaviside step functions with maximum 100% transmission. The flux measured by each filter will be

$$F_r = A + f_{\text{cont}} W_r = A \left( 1 + \frac{W_r}{EW} \right) \quad (\text{B1})$$

and

$$F_{H\alpha_b} = A \left( 1 + \frac{W_{H\alpha_b}}{EW} \right) \quad (\text{B2})$$

By computing the ratio between equations B2 and B1 we manage to cancel out  $A$  and obtain

$$EW = \frac{W_r \times \left( \frac{F_{H\alpha_b}}{F_r} \right) - W_{H\alpha_b}}{1 - \left( \frac{F_{H\alpha_b}}{F_r} \right)}. \quad (\text{B3})$$

Finally we define

$$EW_{ph} = C_1 EW \quad (\text{B4})$$

where we introduce the calibration constant  $C_1$  to account for the non-squared shape of the emission line profile and possible deviations of the filter transmission curves with respect to perfect Heaviside step functions.

**APPENDIX C: PHOTOMETRIC FWHM**

Following from Appendix B we call  $FWHM$  the width of the emission line profile and define a narrow band  $H\alpha$  filter (also with a Heaviside step profile) of equivalent width  $W_{H\alpha_n} < FWHM$ . The flux measured by this filter will be

$$F_{H\alpha_n} = A_n + A \left( \frac{W_n}{EW} \right) \quad (\text{C1})$$

where  $A_n = A \times (W_n / FWHM)$  is the fraction of line flux measured by the narrow  $H\alpha$  filter. By dividing equation C1 by B2 and after some algebra we obtain

$$FWHM = \frac{EW_{ph}}{\left( \frac{EW_{ph} + W_{H\alpha_b}}{W_{H\alpha_n}} \right) \times \left( \frac{F_{H\alpha_n}}{F_{H\alpha_b}} \right) - 1} \quad (\text{C2})$$

As before we define

$$FWHM_{ph} = C_2 FWHM \quad (\text{C3})$$

where the constant  $C_2$  accounts for the non-squared shape of the emission line profile and possible deviations of the

filter transmission curves with respect to perfect Heaviside step functions.

This paper has been typeset from a  $\text{\TeX}/\text{\LaTeX}$  file prepared by the author.